

Robust Point Cloud Registration via Geometric Overlapping Guided Rotation Search

Zhao Zheng, Jingfan Fan, Long Shao, Hong Song, Danni Ai, Tianyu Fu, Deqiang Xiao, Yongtian Wang, and Jian Yang

Abstract—Point cloud registration based on correspondences computes the rigid transformation that maximizes the number of inliers constrained within the noise threshold. Current state-of-the-art (SOTA) methods employing spatial compatibility graphs or branch-and-bound (BnB) search mainly focus on registration under high outlier ratios. However, graph-based methods require at least quadratic space and time complexity for graph construction, while multi-stage BnB search methods often suffer from inaccuracy due to local optima between decomposed stages. This paper proposes a geometric maximum overlapping registration framework via rotation-only BnB search. The rigid transformation is decomposed using Chasles’ theorem into a translation along rotation axis and a 2D rigid transformation. The optimal rotation axis and angle are searched via BnB, with residual parameters formulated as range maximum query (RMQ) problems. Firstly, the top-k candidate rotation axes are searched within a hemisphere parameterized by cube mapping, and the translation along each axis is estimated through interval stabbing of the correspondences projected onto that axis. Secondly, the 2D registration is relaxed to 1D rotation angle search with 2D RMQ of geometric overlapping for axis-aligned rectangles, which is solved deterministically in polynomial time using sweep line algorithm with segment tree. Experimental results on 3DMatch, 3DLoMatch, and KITTI datasets demonstrate superior accuracy and efficiency over SOTA methods, while the time complexity is polynomial and the space complexity increases linearly with the number of points, even in the worst case.

Index Terms—Point cloud registration, branch-and-bound (BnB) search, range maximum query (RMQ), interval stabbing, segment tree.

I. INTRODUCTION

PPOINT cloud registration estimates the rigid transformation with 6 degrees of freedom (DoF) between two point clouds, which is a fundamental problem in simultaneous localization and mapping (SLAM) [1]–[3], computer assisted

This work was supported by the National Science Foundation Program of China (62025104, 62422102, 62331005, U22A2052), the National Key R&D Program of China (2023YFC2415300), and Haidian Original Innovation Joint Fund of Beijing Natural Science Foundation (L242091). (Corresponding Authors: Jingfan Fan; Long Shao; Jian Yang.)

Zhao Zheng, Jingfan Fan, Long Shao, Danni Ai, Deqiang Xiao, Yongtian Wang, and Jian Yang are with Beijing Engineering Research Center of Mixed Reality and Advanced Display, School of Optics and Photonics, Beijing Institute of Technology, Beijing 100081, China, and Zhengzhou Research Institute, Beijing Institute of Technology, Zhengzhou 450003, China (e-mail: fff@bit.edu.cn; lshao@bit.edu.cn; jyang@bit.edu.cn).

Hong Song is with the School of Computer Science and Technology, Beijing Institute of Technology, Beijing 100081, China.

Tianyu Fu is with the School of Medical Technology, Beijing Institute of Technology, Beijing 100081, China.

Code will be available at <https://github.com/Bitzhaozheng/GMOR>.

surgery [4]–[6] and augmented reality [7]–[9]. Although iterative closest point (ICP) [10] and its variants [11]–[13] are widely used for fine registration with given initial alignment, they require robust initialization by employing a global registration method.

Global registration methods estimate the rigid transformation between point clouds by establishing correspondences without initial guesses. Conventional correspondence-based approaches rely on handcrafted geometric primitives, such as 4-points congruent sets [14], [15], convex hull [16], [17] and dense local feature descriptors [18], [19]. While generating plausible correspondences, these methods typically produce significant outlier proportions that necessitate robust filtering. Recently, variants of RANSAC [20], [21], graph-based match [22]–[24], and branch-and-bound (BnB) search [25]–[28] have demonstrated effectiveness in robust global registration against outliers. The exceptional outlier rejection capability of spatial compatibility (SC) from graph-based methods has prompted their integration into other pipelines [21], [29]. Nevertheless, these methods face a critical trade-off: no universal approach simultaneously achieves robustness across varying outlier ratios and correspondence counts while guaranteeing polynomial time and linear space complexity.

To achieve globally optimal point cloud registration with guaranteed space and time complexity, we propose a Geometric Maximum Overlapping Registration (GMOR) framework using two-stage rotation-only BnB search. The method employs Chasles’ decomposition theorem [30] to decouple the rigid transformation, as shown in Fig. 1. The rotation axis is searched by cube mapping parameterization in the first stage and the translation along the axis is estimated by 1D range maximum query (RMQ) of overlapped correspondences projected onto the axis. This 1D RMQ adapts the interval stabbing algorithm used in previous works [26]–[29], [31]. The second stage searches rotation angles in 1D space, where we relax rotation centers determined by angles to axis-aligned bounding boxes. Maximum inlier estimation is formulated as a 2D RMQ problem over pairwise intersecting rectangles. We reformulate this geometric maximum overlapping search as the stabbing counting query of Klee’s rectangle problems [32], [33], solving it efficiently via sweep line algorithm inspired by Bentley-Ottmann algorithm [34] augmented with segment tree. By combining BnB over Special Orthogonal Group (SO(3)) with these computational geometry-based techniques, our approach achieves polynomial time complexity through di-

arXiv:2508.17427v1 [cs.CV] 24 Aug 2025

mension reduction while maintaining linear space complexity. The contributions of our work are as follows:

- A novel two-stage rotation-only BnB framework using Chasles' decomposition guarantees global convergence in polynomial time with linear space complexity, eliminating graph construction overhead.
- Cube-mapped hemispherical parameterization for rotation axis search is coupled with adaptive interval stabbing of translation along the axis, progressively tightening intervals through correspondence projections to accelerate RMQ resolution.
- A deterministic polynomial-time solution for 2D rigid registration is derived by reformulating as 1D rotation angle search with Klee's rectangle counting, which utilizes sweep line algorithm with segment tree in $O(N \log N)$ time per iteration.

II. RELATED WORK

A. Feature extraction and learning-based registration

A common approach for global registration is extracting the corresponding features between two point clouds to estimate the transformation between them. Rusu et al. [18] propose a Fast Point Feature Histograms (FPFH) descriptor for global registration, which is a handcrafted feature capturing the local geometry of each point invariant to scene context. Learning-based feature descriptors have been widely used for specific scenes, and 3DMatch proposed by Zeng et al. [35] is a pioneering work which provides the first benchmark dataset for learned feature representations. Choy et al. [36] propose Fully Convolutional Geometric Features (FCGF), which is trained separately on indoor/outdoor datasets and achieves higher inlier ratio. Huang et al. [37] demonstrate that using pairwise point clouds as joint input extracts richer features, proposing Predator for low-overlap cases. Qin et al. [38] further employ Transformer networks to model global geometric relationships of pairwise point clouds.

Based on the correspondence matching in feature space, the rigid transformation is estimated by either RANSAC [39] or chunk-based methods [38]. Recently, end-to-end learning approaches, e.g. DGR [40] and PointDSC [22], are progressive for solving the rigid transformation of correspondences. While effective in specific scenarios [41], [42], they generalize poorly to practical applications. Crucially, traditional methods [21], [24], [29], [43], [44] without learning now surpass them in accuracy and efficiency through graph or solution space exploration. Given these limitations, this section focuses on heuristic global registration techniques.

B. Iterative Random Sampling

RANSAC [39] is a widely used algorithm for robust estimation with outliers, has inspired numerous variants [20], [21], [45]. Rusu et al. [18] leverage pairwise point distances and Fast Point Feature Histograms (FPFH) descriptor similarities to formulate SAmple Consensus Initial Alignment (SAC-IA), which suppresses outlier influence through finite iterations. Barath and Matas [45] improve sampling efficiency with Graph-Cut

RANSAC (GC-RANSAC), removing outliers by graph cutting with local optimization. Unlike local sampling approaches, Li et al. [20] develop a one-point RANSAC variant using global pairwise distance and a modified Tukey's biweight function for scaled transformation estimation. Shi et al. [21] extend this framework and propose TCF, implementing a three-stage RANSAC process for robust outlier rejection.

While these methods demonstrate strong performance under moderate outlier ratios and sufficient correspondences, their computational complexity becomes exponential when outlier ratio is extremely high. To balance robustness and efficiency, RANSAC [39] is commonly integrated with other constraints, e.g. SC graph, as discussed in subsequent sections.

C. Spatial Compatibility Graph Matching

SC [22]–[24] is a practical measure of the geometric consistency between point clouds after rigid transformation. SC graph is constructed by pair-wise distances between correspondences, and the vertices are connected if the distances difference is less than a threshold. Yang et al. [23] propose SAC-COT by randomly sampling three-point correspondences guided by the SC graph, which generates more reliable correspondences than RANSAC [39]. Based on reliable seeds selection of SC graph in PointDSC [22], Chen et al. [24] eliminate the training procedure and propose SC2-PCR with a second order graph (SOG) to sample the correspondences, later extended to SC2-PCR++ [46] via consensus reselection with one-to-many matching. These works demonstrate traditional SOG matching's superiority over end-to-end approaches.

For outlier pruning, Yang et al. [43] propose TEASER++ that combines truncated least squares estimation with practical maximum clique algorithm [47]. Zhang et al. [44] relax the constraint of the maximum clique in TEASER++ [43] and propose MAC to find the maximal cliques of the SOG. This approach employs modified Bron-Kerbosch algorithm implemented in igraph library [48] with complexity $O(d_v(N-d_v)3^{d_v/3})$, where d_v is the graph degeneracy. While efficient for sparse graphs, maximal clique-based methods approach exponential space and time complexity on recursively searching in dense graphs, which leads to memory limitations reported in [28].

In summary, graph-based methods achieve high accuracy particularly with sparse correspondence sets. However, their applicability is constrained by following primary factors: 1) quadratic space complexity in graph construction limits scalability for large-scale point clouds; 2) clique search exhibits exponential time complexity in the worst case of dense graphs; 3) SC's distance invariance under Euclidean Group (E(3)) rather than Special Euclidean Group (SE(3)) may yield inaccurate registrations under improper rotations.

D. BnB Search in Solution Space

BnB search provides globally optimal solutions for combinatorial optimization problems, but the time complexity increases exponentially in the dimensionality of the solution space. Recent works [25]–[28] focus on the search in the 6-DoF solution space of rigid transformation. Hartley and

Kahl [49] pioneered this approach, formulating rotation search as BnB over the closed ball with radius π in \mathbb{R}^3 using Rodrigues parameterization. Yang et al. [25] propose Go-ICP with nested BnB search of $SE(3)$ to estimate the 6-DoF rigid transformation between two point clouds. To reduce the dimensions of search space, Bustos et al. [50] propose a fast rotation search with circular R-tree indexing, but it still requires the nested \mathbb{R}^3 translation search. In further research, Bustos and Chin [26] propose GORE, combining BnB with 1D interval stabbing for outlier removal while leaving the nested translation search problem unresolved.

Although $SE(3)$ BnB search guarantees global optimality, its computational cost remains prohibitive due to 6-DoF search space complexity. Stage-wise decomposition provides a practical compromise, approximating global optima through sequential subproblems. Chen et al. [27] propose TR-DE via two-stage 3-DoF searches: first solving the 2-DoF rotation axis and 1-DoF translation along the axis through 3D BnB, and then solving the 1-DoF rotation angle and 2-DoF planar translation via nested BnB. This reduces the computational complexity from 6 DoF to 3 DoF, while maintaining near-optimal registration accuracy.

Similarly, the 1D interval stabbing algorithm can be utilized in these decomposed stages to reduce the search dimensions [31]. Li et al. [51] decompose registration into three 2-DoF rotation matrix row vector estimation subproblems, and estimate the 1-DoF translation projection via interval stabbing. Based on the row-vector decomposition, Huang et al. [28] propose TEAR to solve in two stages: first resolving an initial row vector through 2-DoF BnB in spherical space with estimating translation via interval stabbing, then adopting rotation matrix orthogonality constraints between rows to simplify subsequent solution. Huang et al. [29] further enhance this approach with HERE, integrating the SC graph with BnB search. It preprocesses the input correspondences by valid sampling of SC graph and then performs a progressive outlier removal in three-stage BnB search with interval stabbing. Nevertheless, staged BnB search improves efficiency but sacrifices the global optimality: once one of the stages gets trapped in a local optima, it is challenging for the subsequent stages to yield the correct result.

In this paper, our approach is a variant of BnB search that mitigates local optima by top- k rotation axes selection. Compared with the decomposed stages in TR-DE [27], we implement the following key innovations: In stage I, the rotation axis is discretized via spherical cube mapping, and the translation is solved using tighter boundaries with interval stabbing. In stage II, a novel deterministic 2D registration through sweep line algorithm with segment tree compresses the 3-DoF search in TR-DE [27] to 1 DoF, while maintaining registration accuracy.

III. PROBLEM FORMULATION

Given two point clouds with N correspondences $\{\mathbf{P}_i\}_{i=1}^N$ and $\{\mathbf{Q}_i\}_{i=1}^N$, the purpose is to estimate the rotation matrix \mathbf{R}

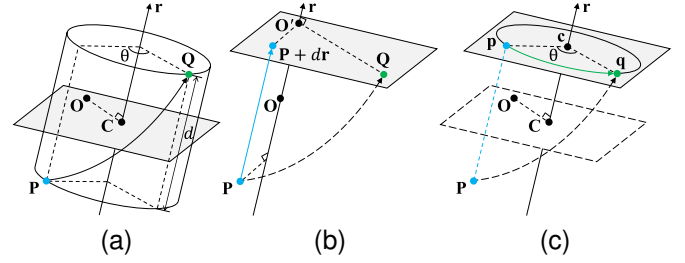


Fig. 1. Decomposition of rigid transformation by Chasles' theorem. (a) Equivalent screw motion from \mathbf{P} to \mathbf{Q} ; (b) Decomposed translation along the rotation axis direction \mathbf{r} ; (c) Residual 2D rotation about the axis through a determined center \mathbf{C} .

and translation vector $\hat{\mathbf{t}}$ that maximize the weighted sum of inliers:

$$\hat{\mathbf{R}}, \hat{\mathbf{t}} = \arg \max_{\mathbf{R}, \mathbf{t}} \sum_{i=1}^N w_i \cdot \mathbb{I}(\|\mathbf{Q}_i - (\mathbf{R}\mathbf{P}_i + \mathbf{t})\| \leq \xi), \quad (1)$$

where $\mathbb{I}(\cdot)$ is the indicator function of inliers, and w_i represents the i^{th} correspondence weight in $\mathbf{w} = \{w_i\}_{i=1}^N$. When $\mathbf{w} = \{1\}^N$, the reduces to the maximizing the inliers count. ξ is the noise threshold, following $\xi^2 = 2\sigma^2\chi_{3,0.95}^2$ from Gaussian noise $\mathcal{N}(0, \sigma^2\mathbf{I})$ per dimension of a single point, with $\chi_{3,0.95}^2$ being the 95% quantile of the 3-DoF chi-square distribution.

As shown in Fig. 1, the rigid transformation is equivalent to a screw motion, which can be decomposed to a translation along the unit rotation axis direction \mathbf{r} and a rotation about the axis through a fixed point \mathbf{C} satisfying $\mathbf{r} \times (\mathbf{R}\mathbf{C} + \mathbf{t} - \mathbf{C}) = \mathbf{0}$. Applying the Rodrigues formula, we reformulate (1) as:

$$\hat{\mathbf{R}}, \hat{\mathbf{t}} = \arg \max_{\mathbf{R}, \mathbf{t}} \sum_{i=1}^N w_i \cdot \mathbb{I}(\|(\mathbf{r} \cdot \mathbf{S}_i - d)\mathbf{r} + \mathbf{r} \times (\mathbf{Q}_i - \mathbf{C} - \mathbf{R}(\mathbf{P}_i - \mathbf{C}))\| \leq \xi), \quad (2)$$

with parameters:

$$\mathbf{S}_i = \mathbf{Q}_i - \mathbf{P}_i, \quad (3a)$$

$$\mathbf{R} = \mathbf{I} \cos \theta + (1 - \cos \theta)\mathbf{r}\mathbf{r}^T + \mathbf{r}_\times \sin \theta, \quad (3b)$$

$$d = \mathbf{r} \cdot \mathbf{t}, \quad (3c)$$

$$\mathbf{C} = \frac{1}{2} \left(\mathbf{I} - \mathbf{r}\mathbf{r}^T + \mathbf{r}_\times \cot \left(\frac{\theta}{2} \right) \right) \mathbf{t}, \quad (3d)$$

where \mathbf{S}_i is the difference vector between \mathbf{Q}_i and \mathbf{P}_i , \mathbf{I} is the identity matrix, \mathbf{r}_\times is the skew-symmetric matrix of unit rotation axis \mathbf{r} , and θ is the rotation angle in the Rodrigues formula (3b). Particularly, \mathbf{C} represents an arbitrary point on the rotation axis with direction \mathbf{r} , and the selected \mathbf{C} in (3d) is the origin point projected onto the axis. It is easy to prove that (2) is equivalent to (1).

Based on the decomposition in (2), we set minimum branch width ϵ and search for the globally optimal rigid transformation through two stages:

- 1) Stage I: BnB search over the hemisphere for rotation axis direction, estimating the translation via interval stabbing of axis-projected correspondences.
- 2) Stage II: BnB search for the rotation angle, estimating the rotation center using sweep line algorithm accelerated by segment tree.

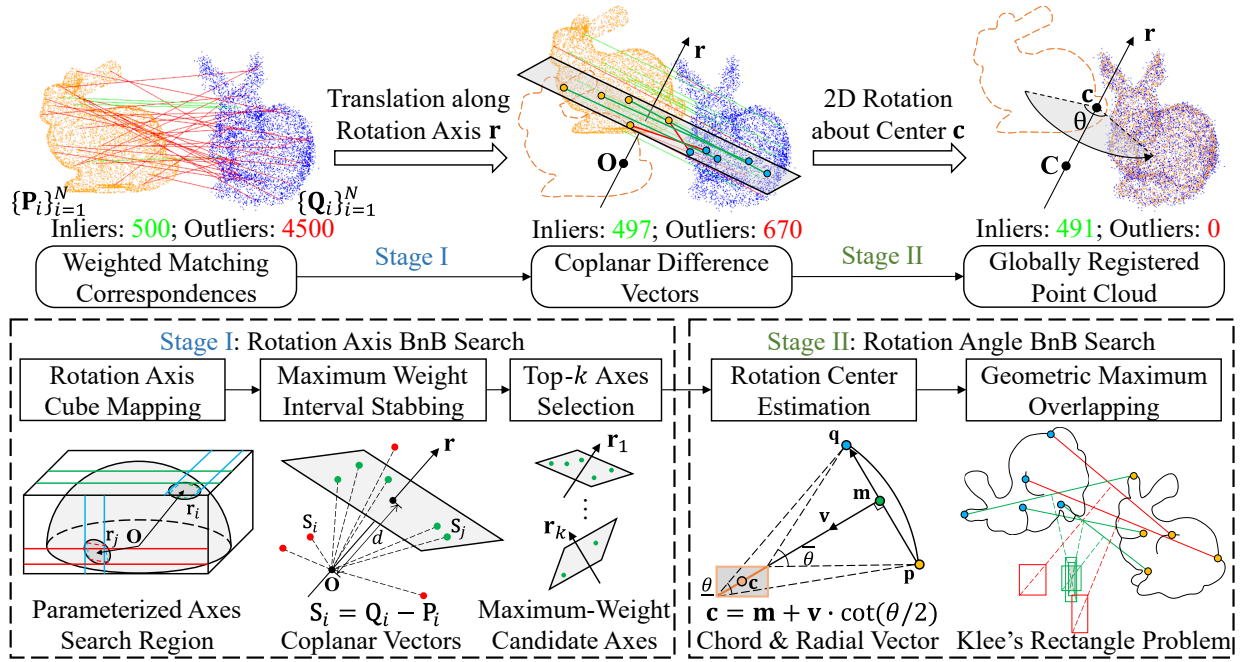


Fig. 2. Two-stage BnB search framework of GMOR.

The framework of our GMOR method is illustrated in Fig. 2. With preprocessed weighted matching, the correspondences are filtered in two stages to maximize the weighted sum of inliers. Furthermore, the subproblem in stage I is selecting maximal-weight coplanar points in 3D space, and the subproblem in stage II is deterministically estimating the rigid transformation on 2D plane.

IV. PREPROCESSING: WEIGHTED CROSS-MATCHING IN FEATURE SPACE

To generate the weighted correspondences between two original point clouds $\{\mathbf{P}_i^o\}_{i=1}^{N_p}$ and $\{\mathbf{Q}_i^o\}_{i=1}^{N_q}$, we perform softmax weighted k-nearest neighbor (kNN) search with dustbin in feature space. The correspondence weights are computed as:

$$w_i = \frac{\exp\left(-\frac{\|\mathbf{f}_i^p - \mathbf{f}_1^q\|^2}{2d_f^2\|\mathbf{f}_i^p\|^2}\right)}{\exp\left(-\frac{\delta^2}{2d_f^2}\right) + \sum_{j=1}^{k_f} \exp\left(-\frac{\|\mathbf{f}_i^p - \mathbf{f}_j^q\|^2}{2d_f^2\|\mathbf{f}_i^p\|^2}\right)}, \quad (4)$$

where \mathbf{f}_i^p and \mathbf{f}_j^q are feature vectors of the i^{th} point in $\{\mathbf{P}_i^o\}_{i=1}^{N_p}$ and j^{th} nearest neighbor in $\{\mathbf{Q}_i^o\}_{i=1}^{N_q}$ respectively. d_f is a distance factor in feature space, and $\delta = \sqrt{2}$ is the dustbin threshold to reduce weights for distant features, and k_f is the number of nearest neighbors. We implement cross-matching by computing the bidirectional kNN from $\{\mathbf{P}_i^o\}_{i=1}^{N_p}$ to $\{\mathbf{Q}_i^o\}_{i=1}^{N_q}$ and vice versa. The combined results form correspondences $\{\mathbf{P}_i\}_{i=1}^N \rightarrow \{\mathbf{Q}_i\}_{i=1}^N$ with weights $\{w_i\}_{i=1}^N$.

V. STAGE I: ROTATION AXIS SEARCH

The stage I objective maximizes inlier weights by finding optimal rotation axis \mathbf{r} and translation distance d :

$$\begin{aligned} \hat{\mathbf{r}}, \hat{d} &= \arg \max_{\mathbf{r}, d} W_1 \\ &= \arg \max_{\mathbf{r}, d} \sum_{i=1}^N w_i \cdot \mathbb{I}(|\mathbf{r} \cdot \mathbf{S}_i - d| \leq \xi_1), \end{aligned} \quad (5)$$

where $\xi_1^2 = 2\sigma^2\chi_{1,0.95}^2$ is the 1D noise threshold.

The objective function (5) identifies the largest coplanar subset of $\{\mathbf{S}_i\}_{i=1}^N$ by fitting a plane with normal \mathbf{r} at distance d from the origin. Unlike TR-DE [27], we parameterize rotation axes via cube mapping [52] on the hemisphere, as shown in Fig. 3(a). The transformation from cube-face coordinates $(x_f, y_f)^T$ (e.g., XY-face) to Cartesian coordinate of rotation axis is

$$\begin{aligned} \mathbf{r}_p &= (x_f, y_f, 1)^T, \\ \mathbf{r} &= \mathbf{r}_p / \|\mathbf{r}_p\|, \end{aligned} \quad (6)$$

where \mathbf{r}_p is the unnormalized rotation axis \mathbf{r} on the cube face. The initial search space per cube face is $[-1, 1] \times [-1, 1]$.

Using hemisphere discretization via cube mapping, we perform 2D BnB search for rotation axis. The rotation axis search employs best-first BnB with space bisection, guided by the upper bound \overline{W}_1 .

A. Projection onto Rotation Axis

The rotation axis \mathbf{r}_c for a surface element is represented by its center $\left(\frac{x_f + \bar{x}_f}{2}, \frac{y_f + \bar{y}_f}{2}\right)^T$. The farthest possible axis \mathbf{r}_m from \mathbf{r}_c lies at the corner closest to the cube

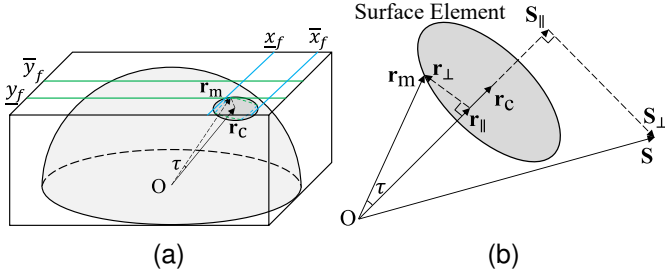


Fig. 3. Rotation axis parameterization for BnB search. (a) Cube mapping with surface element bounding circle. (b) Decomposition of projection onto rotation axis within the surface element.

face center. The translation distance d for correspondence \mathbf{S} projected onto axis \mathbf{r} is:

$$\begin{aligned} d &= \mathbf{r} \cdot \mathbf{S} \\ &= (\mathbf{r}_{\parallel} + \mathbf{r}_{\perp}) \cdot (\mathbf{S}_{\parallel} + \mathbf{S}_{\perp}) \\ &= \mathbf{r}_{\parallel} \cdot \mathbf{S}_{\parallel} + \mathbf{r}_{\perp} \cdot \mathbf{S}_{\perp} \end{aligned} \quad (7)$$

where \mathbf{r} is any axis within the surface element, \mathbf{r}_{\parallel} and \mathbf{r}_{\perp} are components parallel and perpendicular to \mathbf{r}_c , and \mathbf{S}_{\parallel} , \mathbf{S}_{\perp} are corresponding components of \mathbf{S} in Fig. 3(b). The norms of the parallel and perpendicular components satisfy:

$$\begin{aligned} \cos \tau &\leq \|\mathbf{r}_{\parallel}\| \leq 1 \\ 0 &\leq \|\mathbf{r}_{\perp}\| \leq \sin \tau \end{aligned} \quad (8)$$

where τ is the maximum angle between \mathbf{r}_m and \mathbf{r}_c . For each correspondence \mathbf{S} , the projection boundaries on \mathbf{r}_c are:

$$\begin{aligned} \underline{d}_l &= \mathbf{r}_c \cdot \mathbf{S} - \xi_1, \\ \bar{d}_l &= \mathbf{r}_c \cdot \mathbf{S} + \xi_1, \end{aligned} \quad (9)$$

Combining (7) and (8) and considering the two cases where \mathbf{S} crosses or does not cross the surface element, we derive tighter boundaries than TR-DE [27]:

$$\begin{aligned} \underline{d}_u &= d_{\parallel} - d_{\perp} - \xi_1, \\ \bar{d}_u &= \begin{cases} d_{\parallel} + d_{\perp} + \xi_1, & \|\mathbf{S}\| \cos \tau > \mathbf{r}_c \cdot \mathbf{S} \\ \|\mathbf{S}\| + \xi_1, & \|\mathbf{S}\| \cos \tau \leq \mathbf{r}_c \cdot \mathbf{S} \end{cases} \\ \text{s.t. } & \mathbf{r}_c \cdot \mathbf{S} \geq 0 \end{aligned} \quad (10)$$

where $d_{\parallel} = \mathbf{r}_c \cdot \mathbf{S} \cos \tau$ and $d_{\perp} = \|\mathbf{S}_{\perp}\| \sin \tau$.

When $\mathbf{r}_c \cdot \mathbf{S} < 0$, the boundaries in (10) are inverted:

$$\begin{aligned} \bar{d}_u &= d_{\parallel} + d_{\perp} + \xi_1, \\ \underline{d}_u &= \begin{cases} d_{\parallel} - d_{\perp} - \xi_1, & \|\mathbf{S}\| \cos \tau > -\mathbf{r}_c \cdot \mathbf{S} \\ -\|\mathbf{S}\| - \xi_1, & \|\mathbf{S}\| \cos \tau \leq -\mathbf{r}_c \cdot \mathbf{S} \end{cases} \\ \text{s.t. } & \mathbf{r}_c \cdot \mathbf{S} < 0 \end{aligned} \quad (11)$$

B. Gradually Converged Interval Stabbing

The boundaries of translation distance form N intervals $\{\underline{d}_{li}, \bar{d}_{li}\}_{i=1}^N$ and $\{\underline{d}_{ui}, \bar{d}_{ui}\}_{i=1}^N$ respectively. The maximum accumulated inlier weights correspond to the peak interval overlap, as shown in Fig. 4(a) and (b). It can be estimated by interval stabbing algorithm [26] modified by weights: 1) Sort all interval boundaries by d , and assign the i^{th} weight of left interval boundary to $+w_i$, right boundary to $-w_i$ for

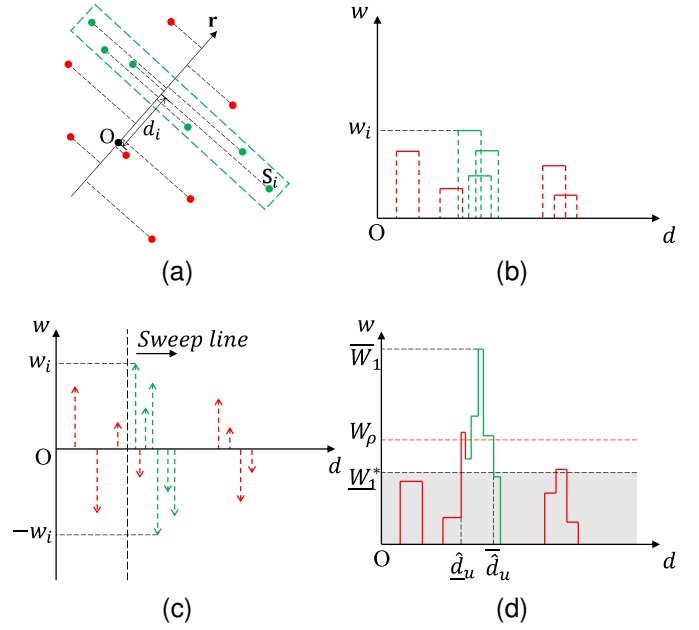


Fig. 4. 1D RMQ solved by interval stabbing. (a) Difference vectors of correspondences projected onto rotation axis. (b) Estimated intervals $[\underline{d}, \bar{d}]$ and weights. (c) Sweep line for traversing discretized left interval boundary with $+w_i$ weight and right with $-w_i$ weight. (d) Accumulated weights and maximum overlapping.

sweep line traversing from left to right, as shown in Fig. 4(c); 2) compute cumulative weights along d -axis, and identify the global maximum in Fig. 4(d).

The upper and lower weights' bounds of the current branch in (5) are estimated using two sets of intervals:

$$\begin{aligned} \bar{W}_1 &= \text{IntervalStabbing} \left(\{[\underline{d}_{ui}, \bar{d}_{ui}]\}_{i=1}^N \right), \\ \underline{W}_1 &= \text{IntervalStabbing} \left(\{[\underline{d}_{li}, \bar{d}_{li}]\}_{i=1}^N \right), \end{aligned} \quad (12)$$

where $\text{IntervalStabbing}(\cdot)$ returns RMQ of the integrated weights. The inlier indices contributing to the peak are not stored during BnB search, but will be reselected based on the optimal rotation axis after search completion.

To accelerate BnB search and prefilter outliers, we implement a gradually converged strategy per branch node: 1) Compute threshold $W_\rho = \rho \bar{W}_1 + (1-\rho) \underline{W}_1^*$ where $0 \leq \rho < 1$, \bar{W}_1 is the current upper bound, and \underline{W}_1^* the global best lower bound; 2) Determine the left interval boundary \hat{d}_u and right boundary \bar{d}_u where accumulated weights exceed W_ρ , as shown in Fig. 4(d); 3) The possible translation distance range $[\hat{d}_u, \bar{d}_u]$ of current branch is inherited to the subbranches, and prefilter the points by $\hat{d}_u \leq \mathbf{r}_c \cdot \mathbf{S} \leq \bar{d}_u$.

In the BnB search, the branch will be pruned in the following cases: 1) Current upper bound \bar{W}_1 is less than the best lower bound \underline{W}_1^* ; 2) The current branch width $\bar{x}_f - \underline{x}_f$ or $\bar{y}_f - \underline{y}_f$ is less than the minimum branch width ϵ ; 3) The current width of upper lower bounds $\bar{W}_1 - \underline{W}_1$ is less than a bound threshold ϵ_b .

C. Post Top- k Plane Fitting

Specifically, while the BnB search result for the rotation axis on the hemisphere yields the optimal solution for stage I, this axis may not correspond to the global optimum for the rigid transformation. We initialize the search by partitioning each cube face into four branches defined by corner coordinates $(0, 0)^T$ and $(\pm 1, \pm 1)^T$. BnB search is then executed independently for each branch. The top- k candidate rotation axes with highest \underline{W}_1 are selected as initial candidates for stage II.

These rotation axes are refined via plane fitting using filtered inliers. The j^{th} fitting plane of inliers $\{\mathbf{S}_i\}_{i=1}^{N_j}$ is estimated through eigenvalue decomposition of the symmetric covariance matrix $\mathbf{\Gamma}_S$:

$$\mathbf{S}_c = \frac{1}{N_j} \sum_{i=1}^{N_j} \mathbf{S}_i, \quad (13a)$$

$$\mathbf{\Gamma}_S = \frac{1}{N_j} \sum_{i=1}^{N_j} (\mathbf{S}_i - \mathbf{S}_c) (\mathbf{S}_i - \mathbf{S}_c)^T = \mathbf{V} \mathbf{D} \mathbf{V}^T, \quad (13b)$$

$$\mathbf{r}_j = \mathbf{v}_3, \quad d_j = \mathbf{r}_j \cdot \mathbf{S}_c, \quad (13c)$$

where \mathbf{S}_c is the centroid of inliers, $\mathbf{V} = [\mathbf{v}_1, \mathbf{v}_2, \mathbf{v}_3]$ contains orthonormal eigenvectors, and $\mathbf{D} = \text{diag}(\lambda_1, \lambda_2, \lambda_3)$ with $\lambda_1 \geq \lambda_2 \geq \lambda_3$. The rotation axis \mathbf{r}_j corresponds to the minimal-variance direction \mathbf{v}_3 , and d_j is the projected centroid distance.

VI. STAGE II: ROTATION ANGLE SEARCH

For each top- k candidate rotation axis from stage I, we project the filtered correspondences onto the plane perpendicular to \mathbf{r} . The problem in stage II then becomes a 2D rigid registration with 3 DoF (1 DoF for the rotation angle and 2 DoF for the translation vector). We efficiently solve this by reducing the search to 1D rotation angle:

- 1) The 2D rigid transformation is a special case where the axial translation is zero in Chasles' theorem, which is equivalent to a rotation about a fixed point.
- 2) The global optimum of 2D rigid transformation can be found in at most $O(\frac{1}{\epsilon} \cdot N \log N)$ time.

Time complexity analysis is detailed in Section VII. As defined previously, the objective function of rotation about a point in stage II is

$$\begin{aligned} \hat{\theta}, \hat{\mathbf{c}} &= \arg \max_{\theta, \mathbf{c}} W_2 \\ &= \arg \max_{\theta, \mathbf{c}} \sum_{i=1}^N w_i \cdot \mathbb{I}(\|(\mathbf{q}_i - \mathbf{c}) - \mathbf{R}_\theta(\mathbf{p}_i - \mathbf{c})\| \leq \xi_2), \end{aligned} \quad (14)$$

where \mathbf{p}_i and \mathbf{q}_i denote the 2D projections of \mathbf{P}_i and \mathbf{Q}_i onto the plane perpendicular to the rotation axis, \mathbf{R}_θ represents the 2D rotation matrix parameterized by angle θ , $\xi_2^2 = 2\sigma^2 \chi_{2,0.95}^2$ defines the noise threshold based on the distribution of distances between two independent 2D points under Gaussian noise, and \mathbf{c} is the rotation center.

Directly BnB searching over the 3-DoF parameter space in (14) is computationally inefficient. To address this issue, we leverage geometric properties of 2D rigid transformations:

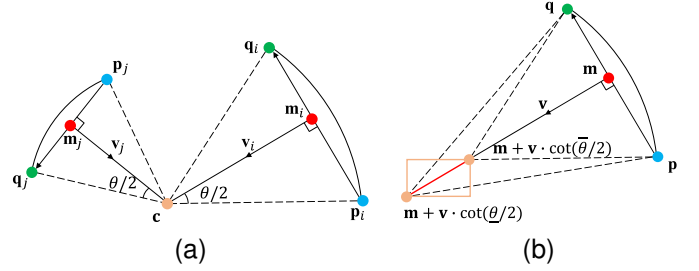


Fig. 5. Rigid transformation on the 2D plane. (a) Chords and arcs for rotation of θ angle about \mathbf{c} . (b) Rotation center determined by $[\theta, \bar{\theta}]$ and correspondence.

We reduce the search to the 1-DoF rotation angle θ , while efficiently estimating the corresponding optimal rotation center \mathbf{c} for each candidate angle using a sweep line algorithm accelerated by a segment tree.

A. Rotation Center Determined by Angle

Given rotation angle θ and center \mathbf{c} , an inlier \mathbf{p} moves along the arc to \mathbf{q} , as shown in Fig. 5(a). The chord midpoint \mathbf{m} and the perpendicular vector \mathbf{v} toward \mathbf{c} are:

$$\begin{aligned} \mathbf{m} &= \frac{1}{2}(\mathbf{q} + \mathbf{p}), \\ \mathbf{v} &= \frac{1}{2} \mathbf{R}_{\frac{\pi}{2}}(\mathbf{q} - \mathbf{p}), \end{aligned} \quad (15)$$

where $\mathbf{R}_{\frac{\pi}{2}}$ is the 2D rotation matrix of 90° . The rotation center \mathbf{c} for given angle θ and chord $\mathbf{p} \rightarrow \mathbf{q}$ is:

$$\begin{aligned} \mathbf{c}(\theta) &= (x_c(\theta), y_c(\theta))^T \\ &= \mathbf{m} + \mathbf{v} \cot\left(\frac{\theta}{2}\right) \\ &= \frac{1}{2} \begin{bmatrix} x_q + x_p - (y_q - y_p) \cot\left(\frac{\theta}{2}\right) \\ y_q + y_p + (x_q - x_p) \cot\left(\frac{\theta}{2}\right) \end{bmatrix}, \end{aligned} \quad (16)$$

where $\mathbf{p} = (x_p, y_p)^T$ and $\mathbf{q} = (x_q, y_q)^T$ are 2D coordinates. Therefore, the range of rotation center \mathbf{c} is determined by the range of angle $[\theta, \bar{\theta}]$ and (16), as shown in Fig. 5(b). Given the prior Gaussian noise σ in each dimension of correspondences, the covariance matrix of \mathbf{c} is derived as:

$$\mathbf{\Gamma}_c = \frac{1}{2} \csc^2\left(\frac{\theta}{2}\right) \sigma^2 \mathbf{I}, \quad (17)$$

where \mathbf{I} is the identity matrix. As a result that the noises of \mathbf{c} in x and y directions are independent, and the prior noise threshold of the rotation center is

$$\xi_c^2(\theta) = \frac{1}{2} \csc^2\left(\frac{\theta}{2}\right) \sigma^2 \chi_{2,0.95}^2. \quad (18)$$

The noise threshold constrains the possible rotation center \mathbf{c} to a circular region centered at $\mathbf{c}(\theta)$ with radius $\xi_c(\theta)$. This geometric constraint is equivalent to the inlier condition in (14), formalized by:

Lemma 1: The rotation center \mathbf{c} within the bounding area determined by $\mathbf{p}, \mathbf{q}, \theta$ and σ satisfies the inequality in the indicator function of (14).

Proof 1: By converting the noise threshold $\xi_c(\theta)$ in x and y dimensions to polar coordinates, the bounding area of \mathbf{c} is rewritten as

$$\begin{aligned} \mathbf{c} &= \mathbf{c}(\theta) + \xi_c(\theta)\mathbf{u}, \\ \text{s.t. } \|\mathbf{u}\| &\leq 1, \end{aligned} \quad (19)$$

where \mathbf{u} is an arbitrary 2D vector within the unit circle. The residual vector in (14) is

$$\mathbf{e} = (\mathbf{q} - \mathbf{c}) - \mathbf{R}_\theta(\mathbf{p} - \mathbf{c}). \quad (20)$$

The rotation center $\mathbf{c}(\theta)$ derived by geometric constraint in (16) follows that $(\mathbf{q} - \mathbf{c}(\theta)) - \mathbf{R}_\theta(\mathbf{p} - \mathbf{c}(\theta)) = \mathbf{0}$, and the norm of residual vector is

$$\|\mathbf{e}\|^2 = \|\xi_c(\theta) (\mathbf{I} - \mathbf{R}_\theta) \mathbf{u}\|^2 \quad (21a)$$

$$= \|\xi_c(\theta) (\mathbf{R}_{\frac{\theta}{2}}^T - \mathbf{R}_{\frac{\theta}{2}}) \mathbf{u}\|^2 \quad (21b)$$

$$= \left\| \xi_c(\theta) \begin{bmatrix} 0 & 2 \sin(\frac{\theta}{2}) \\ -2 \sin(\frac{\theta}{2}) & 0 \end{bmatrix} \mathbf{u} \right\|^2 \quad (21c)$$

$$= 2\sigma^2 \chi_{2,0.95}^2 \left\| \begin{bmatrix} 0 & 1 \\ -1 & 0 \end{bmatrix} \mathbf{u} \right\|^2 \quad (21d)$$

$$= 2\sigma^2 \chi_{2,0.95}^2 \left\| \mathbf{R}_{\frac{\theta}{2}}^T \mathbf{u} \right\|^2 \quad (21e)$$

$$\leq 2\sigma^2 \chi_{2,0.95}^2, \quad (21f)$$

which is equivalent to the inequality with threshold ξ_2 in (14). Therefore, we can solve the problem of rotation center \mathbf{c} with maximum overlapping instead of (14).

For computational convenience in the sweep line algorithm in subsequent sections, we approximate the bounding circle as a square of equivalent area. The half-edge length $\hat{\xi}_c(\theta)$ satisfies:

$$\hat{\xi}_c^2(\theta) = \frac{\pi}{4} \xi_c^2(\theta). \quad (22)$$

Combining (16) and (18), the bounding box corners for angle interval $[\underline{\theta}, \bar{\theta}]$ and correspondence $\{\mathbf{p}, \mathbf{q}\}$ are:

$$\underline{x}_{cu} = \min(x_c(\underline{\theta}) - \hat{\xi}_c(\underline{\theta}), x_c(\bar{\theta}) - \hat{\xi}_c(\bar{\theta})), \quad (23a)$$

$$\bar{x}_{cu} = \max(x_c(\underline{\theta}) + \hat{\xi}_c(\underline{\theta}), x_c(\bar{\theta}) + \hat{\xi}_c(\bar{\theta})), \quad (23b)$$

$$\underline{y}_{cu} = \min(y_c(\underline{\theta}) - \hat{\xi}_c(\underline{\theta}), y_c(\bar{\theta}) - \hat{\xi}_c(\bar{\theta})), \quad (23c)$$

$$\bar{y}_{cu} = \max(y_c(\underline{\theta}) + \hat{\xi}_c(\underline{\theta}), y_c(\bar{\theta}) + \hat{\xi}_c(\bar{\theta})). \quad (23d)$$

Similar to stage I, we compute a bounding box centered at $\theta_c = (\underline{\theta} + \bar{\theta})/2$:

$$\underline{x}_{cl} = x_c(\theta_c) - \hat{\xi}_c(\theta_c), \quad (24a)$$

$$\bar{x}_{cl} = x_c(\theta_c) + \hat{\xi}_c(\theta_c), \quad (24b)$$

$$\underline{y}_{cl} = y_c(\theta_c) - \hat{\xi}_c(\theta_c), \quad (24c)$$

$$\bar{y}_{cl} = y_c(\theta_c) + \hat{\xi}_c(\theta_c). \quad (24d)$$

For each angle interval $[\underline{\theta}, \bar{\theta}]$, the rectangles with $(\underline{x}_{cu}, \underline{y}_{cu}, \bar{x}_{cu}, \bar{y}_{cu})$ are used to estimate the upper bound \bar{W}_2 , and the rectangles with $(\underline{x}_{cl}, \underline{y}_{cl}, \bar{x}_{cl}, \bar{y}_{cl})$ are used to estimate the lower bound \underline{W}_2 .

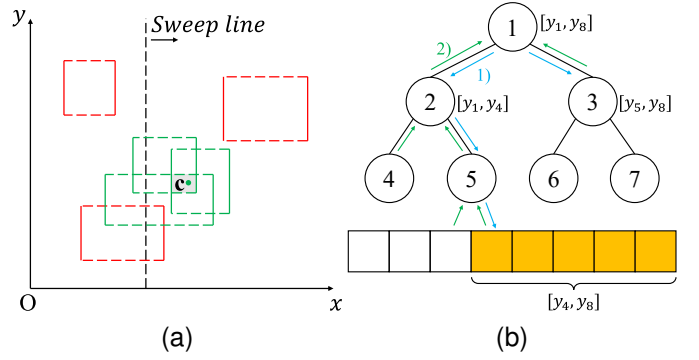


Fig. 6. Rotation center search using sweep line algorithm with segment tree. (a) Sweep line from left to right for traversing the rectangles. (b) Add a new segment to the tree and update the maximum overlapping within $O(\log N)$ time (e.g. a segment $[y_4, y_8]$ is added and only the $1 \rightarrow 2 \rightarrow 5 \rightarrow y_4$ and $1 \rightarrow 3$ paths are updated).

B. Maximum Overlapping via Sweep Line Algorithm

At each rotation angle interval branch $[\underline{\theta}, \bar{\theta}]$, these axis-aligned rectangles form geometric intersections of Klee's rectangle problems. We compute maximum weighted overlap using sweep line algorithm [34] with segment tree, as shown in Fig. 6.

1) *Segments discretization:* The rectangles in (23) and (24) are discretized into vertical segments of left and right edges $(\underline{x}, y, \bar{y}, w)$ and $(\bar{x}, y, \bar{y}, -w)$, respectively, where w is the rectangle weight. The endpoints of segments are sorted by y -coordinate, and we discretize them by sorted indices from bottom to top:

$$\mathbf{s}_l = (x, y_l, y_r, w),$$

$$\mathbf{s}_r = (\bar{x}, y_l, y_r, -w), \quad (25)$$

$$\text{s.t. } 1 \leq y_l < y_r \leq 2N,$$

where \mathbf{s}_l and \mathbf{s}_r are the left and right edges of rectangles, y_l and y_r are sorted integer indices of the y -coordinate. These segments are then sorted by x -coordinate for traversing from left to right in sweep line algorithm.

2) *Segment tree with lazy propagation:* We present an example implementation of a segment tree spanning integer indices $[1, 2N]$ that maintains the maximum overlapping of weighted rectangles, as shown in Algorithm 1. Each node of stores the sorted indices of segment endpoints $[y_l, y_r]$ in (25), current maximum weighted overlap "val", and lazy tag "lazy". During sweep line traversal, lazy propagation accelerates overlap updates by deferring child node modifications until necessary. This reduces update complexity to $O(\log N)$ per segment, as shown in Fig. 6(b).

The root node of the segment tree maintains the maximum weighted overlap at the current sweep line position. Querying this root node provides the maximum swept overlap in $O(1)$ time per iteration. The complete sweep line procedure for maximum overlap of rectangles is detailed in Algorithm 2.

For the current branch in (14), we estimate the upper and

Algorithm 1 Segment tree example for RMQ.

Require: Node \mathbf{n} in the segment tree, segment endpoints (y_l, y_r) , and weight w

```

1: BUILD( $\mathbf{n}, y_l, y_r$ )
2:    $\mathbf{n}.y_l \leftarrow y_l, \mathbf{n}.y_r \leftarrow y_r$ 
3:    $\mathbf{n}.val \leftarrow 0, \mathbf{n}.lazy \leftarrow 0$ 
4:   if  $y_l = y_r$  then
5:     return
6:   end if
7:    $\text{mid} \leftarrow \lfloor (y_l + y_r)/2 \rfloor$ 
8:   BUILD( $\mathbf{n}.left, y_l, \text{mid}$ )
9:   BUILD( $\mathbf{n}.right, \text{mid} + 1, y_r$ )
10:
11: PUSHDOWN( $\mathbf{n}$ )
12:    $\mathbf{n}.left.val \leftarrow \mathbf{n}.left.val + \mathbf{n}.lazy$ 
13:    $\mathbf{n}.left.lazy \leftarrow \mathbf{n}.left.lazy + \mathbf{n}.lazy$ 
14:    $\mathbf{n}.right.val \leftarrow \mathbf{n}.right.val + \mathbf{n}.lazy$ 
15:    $\mathbf{n}.right.lazy \leftarrow \mathbf{n}.right.lazy + \mathbf{n}.lazy$ 
16:    $\mathbf{n}.lazy \leftarrow 0$ 
17:
18: PUSHUP( $\mathbf{n}$ )
19:    $\mathbf{n}.val \leftarrow \max(\mathbf{n}.left.val, \mathbf{n}.right.val)$ 
20:
21: UPDATE( $\mathbf{n}, y_l, y_r, w$ )
22:   if  $\mathbf{n}.y_l \geq y_l$  and  $\mathbf{n}.y_r \leq y_r$  then
23:      $\mathbf{n}.val \leftarrow \mathbf{n}.val + w$ 
24:      $\mathbf{n}.lazy \leftarrow \mathbf{n}.lazy + w$ 
25:   return
26: PUSHDOWN( $\mathbf{n}$ )
27:    $\text{mid} \leftarrow \lfloor (\mathbf{n}.y_l + \mathbf{n}.y_r)/2 \rfloor$ 
28:   if  $(y_l \leq \text{mid})$  then
29:     UPDATE( $\mathbf{n}.left, y_l, y_r, w$ )
30:   end if
31:   if  $(y_r > \text{mid})$  then
32:     UPDATE( $\mathbf{n}.right, y_l, y_r, w$ )
33:   end if
34:   PUSHUP( $\mathbf{n}$ )
    
```

lower weights' bounds via the two rectangle sets:

$$\begin{aligned} \overline{W}_2 &= \text{SweepLine} \left(\left\{ \left(\underline{x}_{cu}, \underline{y}_{cu}, \overline{x}_{cu}, \overline{y}_{cu} \right) \right\}_{i=1}^N \right), \\ \underline{W}_2 &= \text{SweepLine} \left(\left\{ \left(\underline{x}_{cl}, \underline{y}_{cl}, \overline{x}_{cl}, \overline{y}_{cl} \right) \right\}_{i=1}^N \right), \end{aligned} \quad (26)$$

where $\text{SweepLine}(\cdot)$ computes the maximum rectangle overlap in Algorithm 2. The pruning strategy of BnB search follows stage I in Sec. V.

C. Degeneration Induced by Translation-only Problem

When rotation angle $\theta \in [-\epsilon/2, \epsilon/2]$, the rotation center \mathbf{C} in (3d) and noise threshold $\xi_c(\theta)$ diverge, requiring specialized handling.

Under approximation of small rotation angle that $\mathbf{R} \approx \mathbf{I}$, all rotation axes in stage I are correct. The points are filtered by difference vectors $\mathbf{q}_i - \mathbf{p}_i$ on the 2D plane perpendicular to the rotation axes, where inliers should have similar difference

Algorithm 2 Sweep line algorithm with segment tree.

Input: Bounding boxes $\{(\underline{x}_i, \underline{y}_i, \overline{x}_i, \overline{y}_i)\}_{i=1}^N$, weights of correspondences $\{w_i\}_{i=1}^N$

Output: Maximum overlapping of weighted rectangles W_2

```

1: Sort  $\{\underline{y}_i, \overline{y}_i\}_{i=1}^N$  to indices  $\{y_{li}, y_{ri}\}_{i=1}^N$ 
2: Initialize segments  $\{\mathbf{s}_i\}_{i=1}^{2N}$ 
3: for  $i \leftarrow 1$  to  $N$  do
4:    $\mathbf{s}_{2i-1} \leftarrow (\underline{x}_i, y_{li}, y_{ri}, w_i)$ 
5:    $\mathbf{s}_{2i} \leftarrow (\overline{x}_i, y_{li}, y_{ri}, -w_i)$ 
6: end for
7: Sort  $\{\mathbf{s}_i\}_{i=1}^{2N}$  by  $x$ -coordinate
8: Initialize segment tree  $\mathbf{T}, W_2 \leftarrow 0$ 
9: BUILD( $\mathbf{T}.root, 1, 2N$ )
10: for  $i \leftarrow 1$  to  $2N$  do
11:   UPDATE( $\mathbf{T}.root, \mathbf{s}_i.y_l, \mathbf{s}_i.y_r, \mathbf{s}_i.w$ )
12:   if  $\mathbf{T}.root.val > W_2$  then
13:      $W_2 \leftarrow \mathbf{T}.root.val$ 
14:   end if
15: end for
    
```

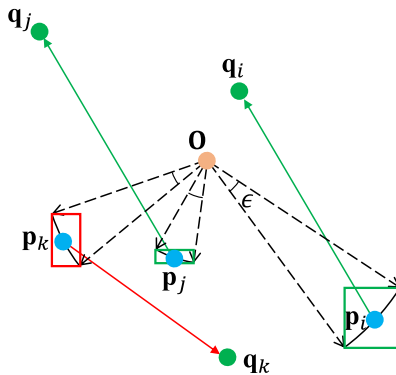


Fig. 7. Translation-only problem with zero rotation angle and the bounding boxes.

vectors, as shown in Fig. 7. Due to the minimum branch width ϵ , the arc can be approximated as a straight line perpendicular to \mathbf{p}_i . Therefore, the corners of the bounding boxes are approximated using ξ_2 from (14) and (22).

Before rotation search, Algorithm 2 solves this case as well, yielding maximum overlap as initial lower bound \underline{W}_2^* for stage II BnB.

D. Post-Refinement with IRLS

After the two-stage BnB search, we refine the rigid transformation using weighted SVD on inliers [40] via iterative reweighted least squares (IRLS). The weights \hat{w} are assigned using Tukey's biweight kernel [53]:

$$\hat{w} = \begin{cases} \left(1 - \frac{e_r^2}{c^2}\right)^2, & e_r < c \\ 0, & e_r \geq c, \end{cases} \quad (27)$$

where e_r is the residual error, $c = 4.685 \times \text{MAD}$, and MAD is the median absolute deviation of inlier residual errors.

Adopting the scale-annealing estimator [20], [21], we filter inliers by $|e_r| \leq \mu_i$ per iteration. The threshold updates with annealing factor $\lambda = 0.5$ in the IRLS iteration as:

$$\mu_{i+1} = (1 - \lambda)\text{MAD} + \lambda\mu_i. \quad (28)$$

The initial threshold $\mu_1 = \xi$ corresponds to (1), with maximum number of iterations set to 5.

VII. SPACE AND TIME COMPLEXITY

In stage I, BnB searches the 2D hemisphere from the best case with $O(\log \frac{1}{\epsilon})$ to the worst case with $O(\frac{1}{\epsilon^2})$ time, and the worst space complexity of nodes is also $O(\frac{1}{\epsilon^2})$. In each branch node of rotation axis, the 1D interval stabbing of correspondences projected onto the axis is sorted in $O(N \log N)$ time, and the maximum inliers of sorted points are filtered in $O(N)$ time. The top- k plane fitting consumes $O(kN)$ time. Note that $k \ll \frac{1}{\epsilon}, N$, the time complexity of stage I is from $O(\log \frac{1}{\epsilon} \cdot N \log N)$ to $O(\frac{1}{\epsilon^2} N \log N)$.

In stage II with the k rotation axes, BnB searches the 1D rotation angle from the best case with $O(k \log \frac{1}{\epsilon})$ to the worst case with $O(\frac{k}{\epsilon})$. The segments are sorted in $O(N \log N)$ time, and maintained by a segment tree containing $O(N)$ nodes. The sweep line algorithm traverses $O(N)$ segments by x , and the maximum overlapping of rectangles is updated in $O(\log N)$ time, leading to $O(N \log N)$ time complexity. Therefore, the time complexity of stage II is from $O(k \log \frac{1}{\epsilon} \cdot N \log N)$ to $O(\frac{k}{\epsilon} N \log N)$.

In summary, the total time complexity with given number of correspondences N and minimum branch width ϵ is from $O(k \log \frac{1}{\epsilon} \cdot N \log N)$ to $O(\frac{1}{\epsilon^2} N \log N)$, and the space complexity is $O(N + \frac{1}{\epsilon^2})$ in the worst case.

VIII. EXPERIMENTAL RESULTS

1) *Datasets and Metrics:* We use real and synthetic datasets to compare our method with other baselines. Specifically, the indoor 3DMatch and 3DLoMatch datasets [35], and outdoor KITTI dataset [54], are employed to evaluate the real-data performance of the baseline methods. Additionally, synthetic datasets generated from models of the Stanford 3D Scanning Repository [55] are used in further experiments with arbitrary number of correspondences and outlier ratio.

Following [56], the rotation error (RE) between the estimated rotation matrix $\hat{\mathbf{R}}$ and the ground truth \mathbf{R} is computed using chordal distance. The translation error (TE) is defined as the Euclidean distance between $\hat{\mathbf{t}}$ and \mathbf{t} :

$$\begin{aligned} \text{RE} &= \arccos \left(\frac{1}{2} \left(\text{tr} \left(\hat{\mathbf{R}}^T \mathbf{R} \right) - 1 \right) \right) \\ &= 2 \arcsin \left(\frac{1}{2\sqrt{2}} \left\| \hat{\mathbf{R}} - \mathbf{R} \right\|_F \right), \\ \text{TE} &= \left\| \hat{\mathbf{t}} - \mathbf{t} \right\|_2, \end{aligned} \quad (29)$$

where $\|\cdot\|_F$ is Frobenius norm, and $\|\cdot\|_2$ is Euclidean distance. A registration is successful if both RE and TE are below a certain threshold. The ratio of successful registrations in all pairs is defined as the registration recall (RR). In our experiments, we report the average RE and TE of successful pairs.

2) *Implementation details:* Our method is implemented in C++ using the Eigen library [57] and accelerated by multi-threading. The feature matching is performed using the Point Cloud Library (PCL) [58] and the nanoflann library [59]. The minimum branch width ϵ is set to 0.05 and the bound threshold ϵ_b is set to 10^{-3} for both our method and TR-DE [27], while the convergence ratio ρ is fixed at 0.25 for our method. For all evaluated methods, we set the inlier distance threshold ξ as twice the downsampling voxel size. All experiments were executed on a laptop with an Intel Core i9-14900HX CPU and 16 GB RAM.

We compare our method with the following baselines on real and synthetic datasets: 1) RANSAC [39] and its variant TCF [21], where RANSAC-1M and RANSAC-4M use a maximum of 10^6 and 4×10^6 iterations respectively; 2) graph-based methods: TEASER++ [43], SC2-PCR++ [46] and MAC [44]; 3) BnB-based methods: TEAR [28], HERE [29] and TR-DE [27]. Since TR-DE [27] also adopts a two-stage BnB search but is closed-source, we re-implement it for fair comparisons. The RANSAC implementation uses Open3D [60] in Python with multi-threading acceleration, and convergence parameters match the official FCGF [36] configuration. As SC2-PCR++ [46] is GPU-optimized whereas others are CPU-based, we adapt its source code for CPU execution following [29]. For multithreaded methods, the thread count is fixed at 12.

Moreover, implementations of RANSAC [39] in Open3D [60], TEASER++ [43], SC2-PCR++ [46], and MAC [44] provide their own feature matching methods. We use the default parameters to reproduce the results. As TEASER++ [43] provides cross checker to reject correspondences in feature space, we observed lower RR compared to configurations without this filter. Consequently, we disable this cross checker by default. For other methods, the features are matched by our preprocessing procedure in Section IV.

A. Indoor 3DMatch and 3DLoMatch Evaluation

For the indoor 3DMatch and 3DLoMatch datasets, we evaluate the methods using feature descriptors extracted by: traditional FPFH [18], learning-based FCGF [36], and Predator [37]. Considering the distribution of different feature extraction methods in feature space, the preprocessing distance factor d_f is set to 0.01 for FPFH [18], 0.07 for FCGF [36] and 0.05 for Predator [37], and the number of kNN searched features k_f is set to 40 for FPFH [18], 60 for FCGF [36] and 30 for Predator [37], respectively. The top- k parameter defaults to 12 for our method. The registration is successful if $\text{RE} < 15^\circ$ and $\text{TE} < 30$ cm.

1) *3DMatch Dataset:* We downsample the point clouds by 5 cm voxel size following [36] and evaluate the methods on 3DMatch dataset with FPFH [18] and FCGF [36] descriptors. Table I shows the results.

With FPFH [18] descriptors, our method outperforms all baselines by over 2% in terms of RR. Both MAC [44] and SC2-PCR++ [46] achieve suboptimal RR, but require $7 \times$ and $60 \times$ more computation time than our method, respectively.

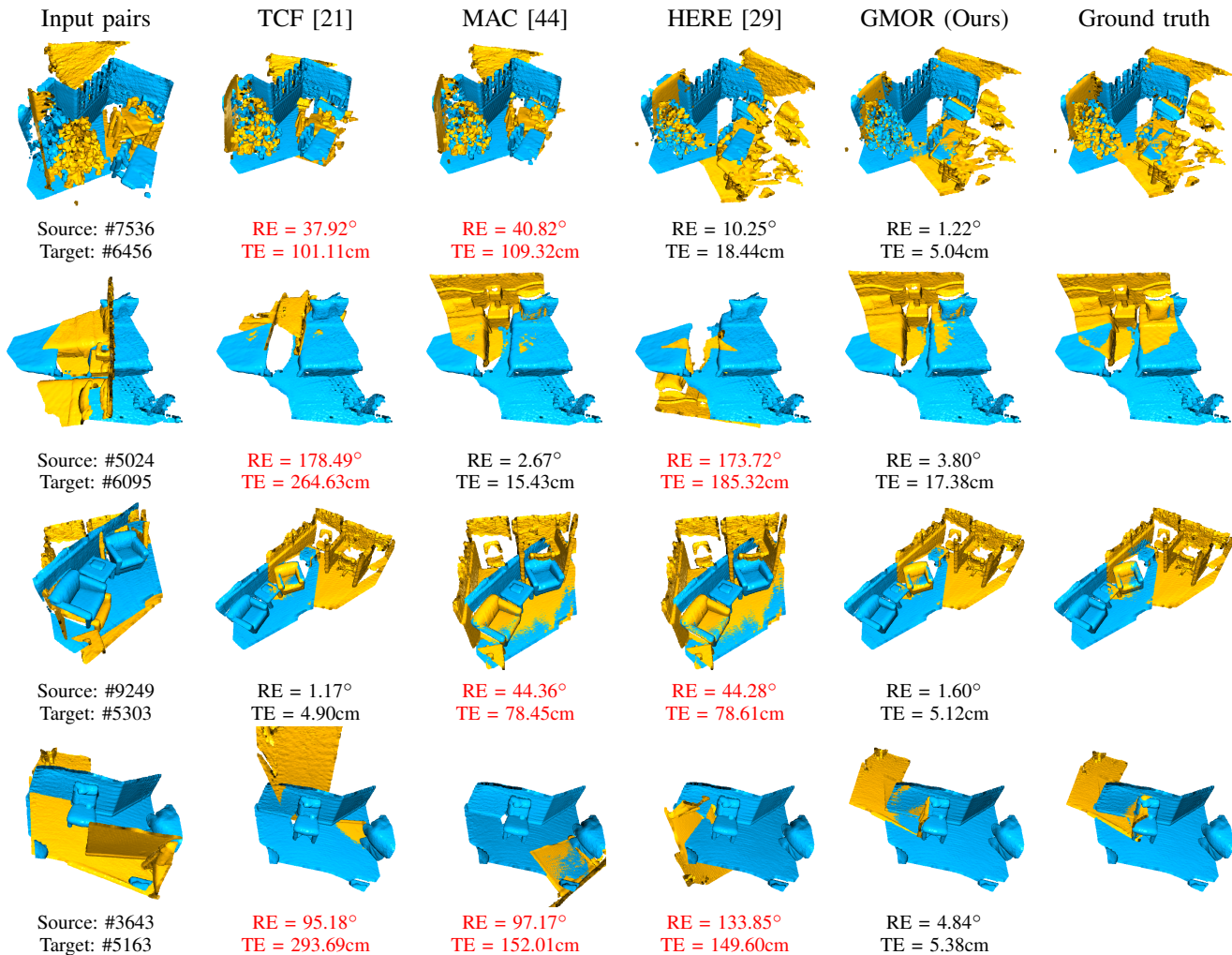


Fig. 8. Visualization of RANSAC-based TCF [21], graph-based MAC [44], BnB-based HERE [29], and our method on the indoor 3DMatch/3DLoMatch datasets using PFPH descriptor [18]. “#” is the number of points, and red text represents the failure case.

The re-implemented TR-DE [27] is the fastest and more efficient than the original paper, but it is less accurate than recent SOTA methods except for TEASER++ [43] and TEAR [28].

Due to the large number of correspondences generated by FCGF [36], TEASER++ [43] requires over 2 hours to compute the maximum clique in some cases. Consequently, we enable its cross checker to reject most correspondences and display the corresponding time in gray in Table I. SC2-PCR++ [46] benefits from its one-to-many feature matching, which increases the likelihood of resampling correct correspondences. This approach reduces FCGF’s [36] generalization error influence but incurs higher computational costs. Notably, SC2-PCR++ [46] achieves higher performance with learning-based descriptors than with traditional descriptors. This performance difference occurs because SC2-PCR++ [46] constructs feature graphs using normalized features, losing information from unnormalized PFPH [18] features during consensus set selection. Our method achieves suboptimal RR and the lowest RE and TE, with significantly reduced computation time compared to SC2-PCR++ [46] on identical hardware.

2) *3DLoMatch Dataset*: The 3DLoMatch dataset is a challenging benchmark for registration with low overlap firstly

TABLE I
QUANTITATIVE RESULTS ON 3DMATCH DATASET.

	FPFH (traditional)			Time(s)↓
	RR(%)↑	RE(°)↓	TE(cm)↓	
RANSAC-1M [39]	62.66	3.72	10.74	0.87
RANSAC-4M [39]	71.97	3.73	10.95	1.94
TCF [21]	86.51	2.66	7.88	9.46
TEASER++ [43]	80.53	3.38	10.87	12.15
SC2-PCR++ [46]	87.31	2.12	6.68	48.33
MAC [44]	87.31	2.37	7.36	5.09
TEAR [28]	61.44	2.80	8.06	0.72
HERE [29]	85.21	2.32	7.05	0.73
TR-DE* [27]	83.49	2.55	7.75	0.38
GMOR (Ours)	89.46	2.29	7.13	0.62
	FCGF (learning-based)			Time(s)↓
	RR(%)↑	RE(°)↓	TE(cm)↓	
RANSAC-1M [39]	84.53	3.40	10.63	0.30
RANSAC-4M [39]	84.78	3.42	10.82	0.52
TCF [21]	89.59	2.25	6.98	33.25
TEASER++ [43]	85.03	2.99	9.51	0.08
SC2-PCR++ [46]	94.15	2.04	6.50	51.30
MAC [44]	92.42	2.05	6.41	19.96
TEAR [28]	83.36	2.31	6.83	0.95
HERE [29]	90.63	2.02	6.32	0.71
TR-DE* [27]	91.44	2.15	6.84	0.25
GMOR (Ours)	93.22	1.90	6.16	0.50

*TR-DE runs with the reproduced code of original work [27].

proposed by Predator [37]. We evaluate the compared methods using FPFH [18] and Predator [37] descriptors. The pre-trained weights provided by Predator [37] employ 2.5 cm voxel size downsampling, differing from the 5 cm voxel size used for other descriptors. Following [46], we downsample each point cloud to 5000 points using the saliency score of Predator [37].

TABLE II
QUANTITATIVE RESULTS ON 3DLoMATCH DATASET.

	FPFH (traditional)			Time(s)↓
	RR(%)↑	RE(°)↓	TE(cm)↓	
RANSAC-1M [39]	10.67	5.52	12.50	<u>0.65</u>
RANSAC-4M [39]	15.61	5.50	13.59	2.38
TCF [21]	43.96	4.28	12.63	3.76
TEASER++ [43]	33.86	4.97	14.79	1.86
SC2-PCR++ [46]	41.66	<u>3.85</u>	10.06	31.19
MAC [44]	49.13	4.00	12.22	2.12
TEAR [28]	13.76	4.33	12.18	1.75
HERE [29]	38.97	3.84	<u>11.52</u>	0.82
TR-DE [27]	43.12	4.09	12.84	0.47
GMOR (Ours)	50.59	3.89	12.01	<u>0.65</u>
	Predator (learning-based)			Time(s)↓
	RR(%)↑	RE(°)↓	TE(cm)↓	
RANSAC-1M [39]	65.36	3.58	10.47	<u>0.46</u>
RANSAC-4M [39]	66.59	3.53	10.28	1.35
TCF [21]	66.37	3.25	10.50	36.32
TEASER++ [43]	61.76	3.54	10.57	0.03
SC2-PCR++ [46]	71.53	3.49	<u>9.78</u>	43.46
MAC [44]	69.17	3.42	10.47	30.24
TEAR [28]	54.41	3.24	10.09	1.27
HERE [29]	64.18	2.98	9.75	1.17
TR-DE [27]	64.85	3.06	10.30	0.36
GMOR (Ours)	<u>69.68</u>	<u>3.02</u>	10.01	0.51

Table II shows the results on the 3DLoMatch dataset. With FPFH [18] descriptors, both MAC [44] and our method surpass other approaches significantly, resulting from their ability to find multiple candidate solutions under low overlap ratios. Besides, maximal clique-based TEASER++ [43] and MAC [44] exhibit faster performance on 3DLoMatch than on 3DMatch. Because the SC graph of correspondences grows sparser given 3DLoMatch’s lower inlier ratios. In contrast, the performance of SC2-PCR++ [46] underperforms on 3DLoMatch relative to 3DMatch though it is also graph-based method. Its SOG sampling yields numerous invalid samples due to FPFH’s [18] low inlier ratios. Our method achieves the highest RR and the suboptimal time consumption. It registers the input point cloud pairs within a stable time (0.62 s on 3DMatch and 0.65 s on 3DLoMatch dataset), regardless of the overlap ratio. In addition, the visualization of the registration results using FPFH [18] descriptor is shown in Fig. 8. Our method maintains accuracy even in challenging cases with repetitive geometries and low overlap.

The results using Predator [37] are similar to those of FCGF [36] descriptor. Downsampling correspondences to 5000 points using Predator’s [37], saliency scores significantly increases the inlier ratio compared to whole point clouds, as verified in [37]. The RR of our method is also the suboptimal with 0.51 s time consumption, comparable to FCGF’s [36] 0.50 s. A more comprehensive ablation study is elaborated in the next section.

3) *Ablation Study on 3DMatch/3DLoMatch*: We conduct a longitudinal study on 3DMatch/3DLoMatch datasets to ana-

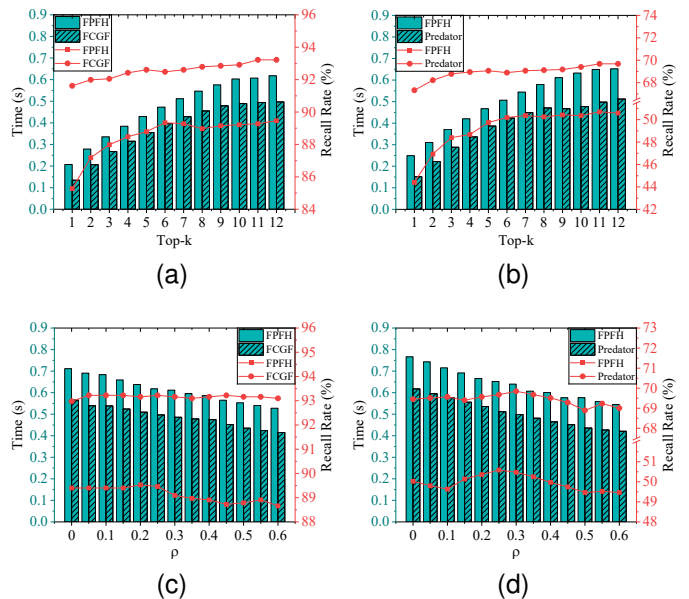


Fig. 9. Ablation study on 3DMatch and 3DLoMatch datasets. (a) 3DMatch with top- k rotation axes; (b) 3DLoMatch with top- k rotation axes; (c) 3DMatch with convergence ratio ρ ; (d) 3DLoMatch with convergence ratio ρ .

lyze top- k rotation axes and convergence ratio ρ . Parameter sweeps vary top- k from 1 to 12 at fixed $\rho = 0.25$ and ρ from 0 to 0.6 at fixed $k = 12$, as shown in Fig. 9.

Both parameters significantly affect computation time. Increasing k yields sublinear time growth while improving RR. FPFH stabilizes at $k > 6$ on both datasets, FCGF improves until $k = 11$, and Predator stabilizes at $k > 4$. This is because the selected k rotation axes between stage I and stage II mitigate the impact of local optima to boost the accuracy. The RR peaks at specific ρ values: 89.53% RR with $\rho = 0.2$ for FPFH [36] on 3DMatch dataset; 50.59% RR with $\rho = 0.25$ for FPFH [36] and 69.85% RR with $\rho = 0.3$ for Predator [37] on 3DLoMatch dataset. Especially for $\rho \in [0.05, 0.60]$, FCGF [36] maintains RR between 93.09% and 93.22%. Although intuition suggests higher RR with smaller ρ , a larger ρ pre-filters more potential outliers, improving both accuracy and efficiency.

B. Outdoor KITTI Evaluation

Following [36], we evaluate compared methods using 555 pairs from KITTI test dataset (sequences 8 to 10). Traditional FPFH [18] and learning-based FCGF [36] descriptor are employed. Particularly, FCGF [36] provides normalized and non-normalized 32-dimensional pre-trained features at 30 cm resolution, and we report the results of normalized version. To ensure predictable execution time and manageable memory consumption, each point cloud is randomly downsampled to 8000 points for pairwise registration. Under the Atlanta World assumption [61] that is already applied to LiDAR point cloud [62], we constrain rotation axis search to the cube face with normal of z -axis, and set top- k to 1. The preprocessing distance factor d_f of feature matching is set to 0.05 and the number of kNN searched features k_f is set to 10 for both

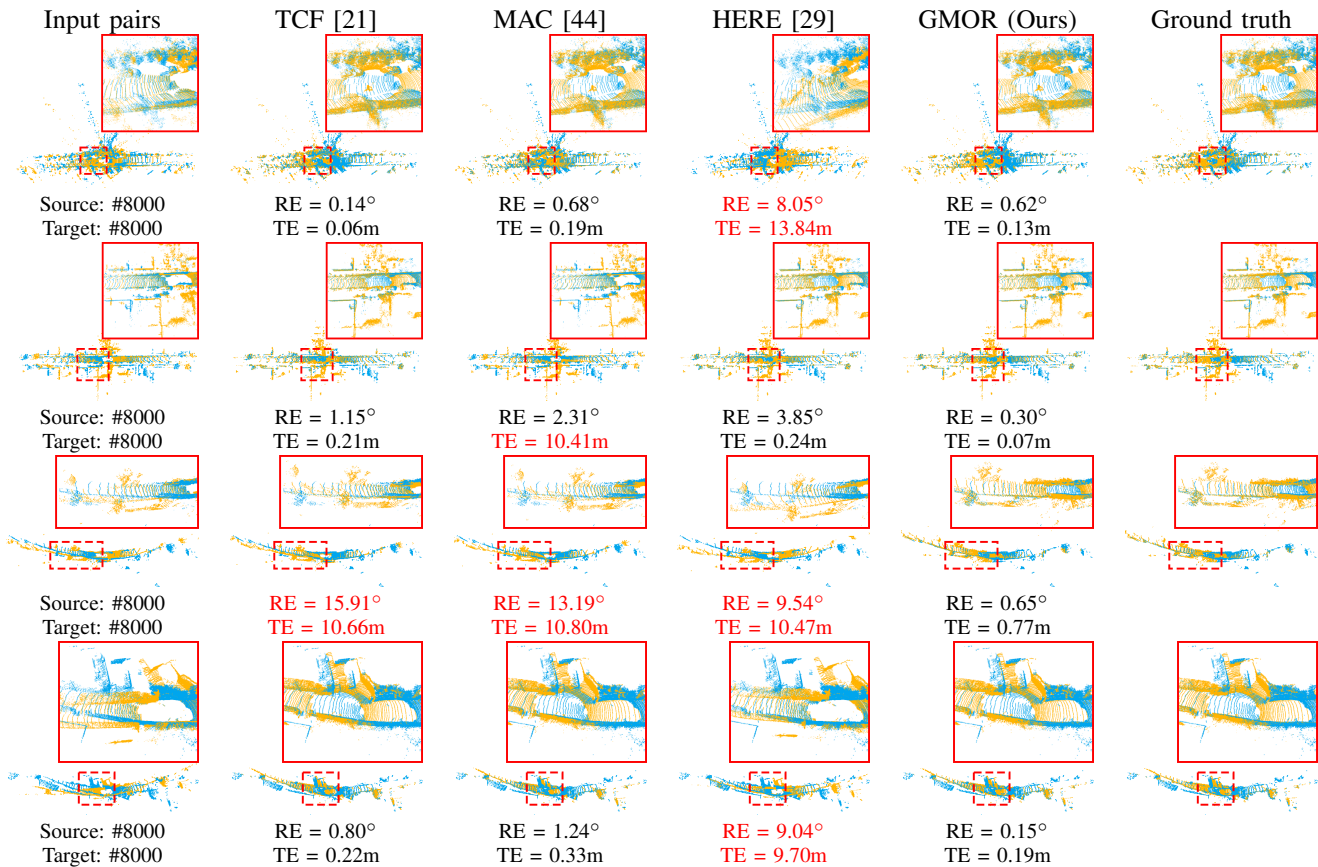


Fig. 10. Visualization of RANSAC-based TCF [21], graph-based MAC [44], BnB-based HERE [29], and our method on the outdoor KITTI dataset using FPFH descriptor [18]. “#” is the number of downsampled points, and red text represents the failure case.

FPFH [18] and FCGF [36] descriptors. The registration is successful if $RE < 5^\circ$ and $TE < 1$ m.

TABLE III
QUANTITATIVE RESULTS ON KITTI DATASET.

	FPFH (traditional)			Time(s)↓
	RR(%)↑	RE(°)↓	TE(cm)↓	
RANSAC-1M [39]	83.24	0.76	24.26	0.62
RANSAC-4M [39]	94.59	0.55	20.41	2.46
TCF [21]	99.82	0.50	11.10	5.19
TEASER++ [43]	99.64	0.37	9.55	3.33
SC2-PCR++ [46]	100.00	0.32	7.19	42.27
MAC [44]	99.10	0.32	7.98	6.43
TEAR [28]	93.69	0.38	9.94	1.83
HERE [29]	99.46	0.31	7.69	1.12
TR-DE [27]	98.02	0.46	11.20	1.61
GMOR (Ours)	100.00	0.24	6.55	0.19
	FCGF (learning-based)			Time(s)↓
	RR(%)↑	RE(°)↓	TE(cm)↓	
RANSAC-1M [39]	99.10	0.33	13.99	0.34
RANSAC-4M [39]	99.28	0.32	13.83	0.39
TCF [21]	99.28	0.31	20.52	24.71
TEASER++ [43]	99.10	0.29	22.08	5.36
SC2-PCR++ [46]	99.46	0.32	20.61	205.06
MAC [44]	98.20	0.31	16.38	5.44
TEAR [28]	96.04	0.36	21.27	0.41
HERE [29]	99.28	0.27	19.03	1.90
TR-DE [27]	99.10	0.34	20.34	0.79
GMOR (Ours)	99.46	0.21	16.14	0.12

Table III reports the evaluation results. Our method achieves the highest RR and the fastest execution with both FPFH [18] and FCGF [18] descriptors on KITTI test dataset. This ef-

iciency advantage stems from the single top- k rotation axis constraints and the restricted search range. SC2-PCR++ [46] achieves competitive RR but incurs the highest time cost due to SOG resampling. On account of the numerous candidate groups of FCGF [36], TCF [21] requires much more time than others to reach the 0.99 confidence. Unexpectedly, RANSAC [39] achieves higher RR with FCGF than with FPFH, contrasting with others’ lower RR using FCGF [36]. This occurs because the RANSAC [39] implemented in Open3D optimizes point cloud overlap, aligning with the triplet loss used in FCGF [36]. The visualization of registration results using FPFH descriptor [18] is shown in Fig. 10, demonstrating that our method achieves accurate registration even in extreme narrow-road LiDAR scenarios.

C. Performance Evaluation on Synthetic Data

To validate the robustness, space and time complexity of our method versus SOTA methods, we evaluate them with varying number of correspondences and outlier ratio. The Armadillo model from the Stanford 3D Scanning Repository [55] serves as synthetic data. This model consists of 172974 points, and we downsample to $N \in \{1000, 5000, \dots, 100000\}$ correspondences. Point clouds are normalized to a $[-1, 1]^3$ m cube before adding zero-mean Gaussian noise and outliers. For the outlier ratio, we randomly generate points in a 10 m diameter sphere, and replace the target points with a probability equal to outlier ratio. Noise magnitude and inlier threshold ξ (set to 0.1)

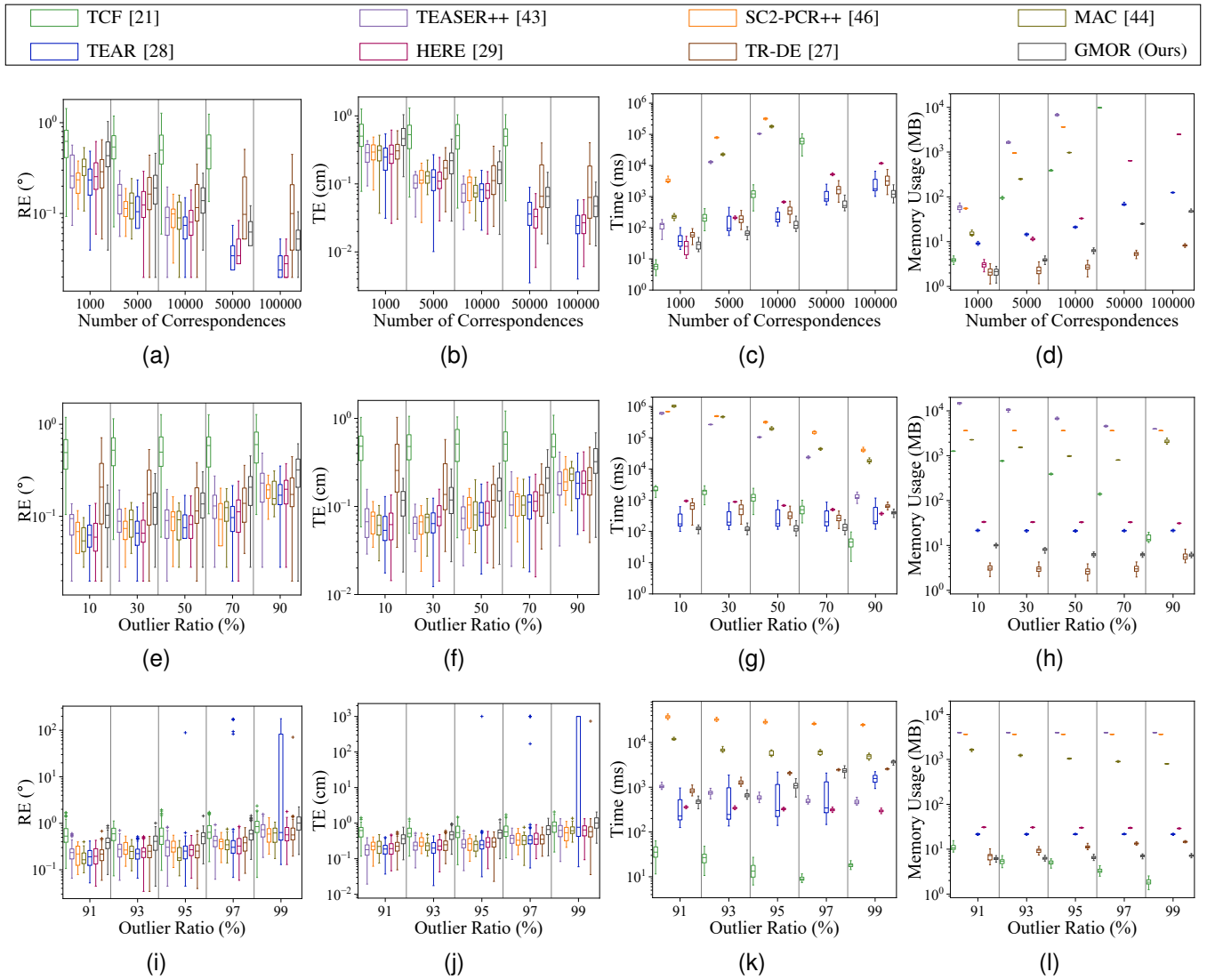


Fig. 11. Performance evaluation of compared SOTA methods with varying numbers of correspondences and outlier ratios on synthetic data. (a)-(d) Number of correspondences; (e)-(h) Outlier ratio; (i)-(l) Extreme outlier ratio.

correspond to Eq. (1). We record the estimated RE and TE, elapsed time and memory usage of compared methods across number of correspondences and outlier ratios in synthetic experiments.

1) *Number of correspondences*: The number of correspondences increases from 1000 to 100000 with 50% outliers across 100 repetitions. The reported memory usage represents the memory allocated by the methods, excluding runtime overhead and data loading. Besides, we modify the source code of HERE [29] to dynamically allocate bitmask matrices, replacing static allocation for accurate measurement.

Fig. 11(a)-(d) show the results across varying number of correspondences. The estimated error decreases for all the methods as the number increases. TCF [21], TEASER++ [43], MAC [44] and SC2-PCR++ [46] exhibit significantly higher time consumption than our method with large number of correspondences. The memory usage increases linearly with the number of correspondences for TEAR [28], TR-DE [27] and our method, but polynomially

for TCF [21], TEASER++ [43], MAC [44] and HERE [29]. TEASER++ [43], SC2-PCR++ [46] and MAC [44] suffer from out-of-memory (OOM) errors beyond 50000 correspondences, while TCF [21] fails at 100000. Our method maintains memory under 100 MB at 100000 correspondences.

2) *Outlier ratio*: We evaluate performance across outlier ratios from 0.1 to 0.9 with 10000 correspondences, and the results are reported in Fig. 11(e)-(h). TCF [21] consumes much more time and memory when the outlier ratio is low, and it exhibits the highest error since IRLS converges slower than Ordinary Least Squares (OLS) under ideal Gaussian noises in our synthetic environment. Similarly, the graph-based TEASER++ [43], MAC [44], SC2-PCR++ [46] incur substantial overhead due to dense graph construction and recursive search. Our method maintains near-optimal time/memory efficiency while ensuring robustness across outlier ratios.

Furthermore, an independent experiment with extreme outlier ratio from 0.91 to 0.99 is also conducted, and the reported results are shown in Fig. 11(i)-(l). Not a number (NaN)

rotation errors are set to 180° , translation errors to 10 m. Failure cases appear in TEAR [28] and TR-DE [27], while other methods succeed. The time advantage of our method narrows in BnB worst-case scenarios, while the graph-based methods gain efficiency. Specifically, TCF [21] has the best performance of time and memory with extreme outlier ratio via one-point RANSAC outlier prefiltering. Our method maintains constant memory usage and achieves the suboptimal performance. In summary, our method demonstrates consistent robustness, efficiency, and low memory consumption across numbers of correspondences and outlier ratios, ensuring predictable time and memory growth in practical applications.

IX. CONCLUSION

In this work, we propose a novel computational geometry-based point cloud registration method named GMOR, which combines BnB search strategy in parameter space and the solution of geometric maximum overlapping formulated as RMQ problem. To ensure the polynomially bounded time complexity and linear space complexity with respect to the number of correspondences, we decompose the search into two stages: rotation axis search with interval stabbing for 1D RMQ, and rotation angle search with sweep line algorithm for 2D RMQ. Experimental results on real and synthetic data demonstrate that our approach achieves efficient and robust registration with low computational overhead, showing potential in lightweight robotics and computer vision applications.

REFERENCES

- [1] C. Bai, T. Xiao, Y. Chen, H. Wang, F. Zhang, and X. Gao, "Faster-LIO: lightweight tightly coupled lidar-inertial odometry using parallel sparse incremental voxels," *IEEE Robot. Autom. Lett.*, vol. 7, no. 2, pp. 4861–4868, 2022.
- [2] J. Ruan, B. Li, Y. Wang, and Y. Sun, "Slamesh: real-time lidar simultaneous localization and meshing," in *Proc. IEEE Int. Conf. Robot. Autom. (ICRA)*. London, United Kingdom: IEEE, 2023, pp. 3546–3552.
- [3] C. Wu, Y. You, Y. Yuan, X. Kong, Y. Zhang, Q. Li, and K. Zhao, "Voxelmap++: mergeable voxel mapping method for online lidar-inertial odometry," *IEEE Robot. Autom. Lett.*, vol. 9, no. 1, pp. 427–434, 2024.
- [4] L. Li, X. Li, B. Ouyang, H. Mo, H. Ren, and S. Yang, "Three-dimensional collision avoidance method for robot-assisted minimally invasive surgery," *Cyborg Bionic Syst.*, vol. 4, p. 0042, 2023.
- [5] W. Li, J. Fan, S. Li, Z. Zheng, Z. Tian, D. Ai, H. Song, X. Chen, and J. Yang, "An incremental registration method for endoscopic sinus and skull base surgery navigation: from phantom study to clinical trials," *Med. Phys.*, vol. 50, no. 1, pp. 226–239, 2023.
- [6] X. Duan, D. Xie, R. Zhang, X. Li, J. Sun, C. Qian, X. Song, and C. Li, "A novel robotic bronchoscope system for navigation and biopsy of pulmonary lesions," *Cyborg Bionic Syst.*, vol. 4, p. 0013, 2023.
- [7] L. Shao, S. Yang, T. Fu, Y. Lin, H. Geng, D. Ai, J. Fan, H. Song, T. Zhang, and J. Yang, "Augmented reality calibration using feature triangulation iteration-based registration for surgical navigation," *Comput. Biol. Med.*, vol. 148, p. 105826, 2022.
- [8] Y. Qin, P. Geng, Y. You, M. Ma, H. Wang, and J. Han, "Collaborative preoperative planning for operation-navigation dual-robot orthopedic surgery system," *IEEE Trans. Automat. Sci. Eng.*, vol. 21, no. 3, pp. 2949–2960, 2024.
- [9] X. Wang, S. Guo, Z. Xu, Z. Zhang, Z. Sun, and Y. Xu, "A robotic teleoperation system enhanced by augmented reality for natural human-robot interaction," *Cyborg Bionic Syst.*, vol. 5, p. 0098, 2024.
- [10] P. Besl and N. D. McKay, "A method for registration of 3-d shapes," *IEEE Trans. Pattern Anal. Mach. Intell.*, vol. 14, no. 2, pp. 239–256, 1992.
- [11] A. L. Pavlov, G. W. Ovchinnikov, D. Y. Derbyshev, D. Tsetserukou, and I. V. Oseledets, "Aa-icp: iterative closest point with anderson acceleration," in *Proc. IEEE Int. Conf. Robot. Autom. (ICRA)*. Brisbane, QLD: IEEE, 2018, Conference Paper, pp. 3407–3412.
- [12] K. Koide, M. Yokozuka, S. Oishi, and A. Banno, "Voxelized gicp for fast and accurate 3d point cloud registration," in *Proc. IEEE Int. Conf. Robot. Autom. (ICRA)*. Xi'an, China: IEEE, 2021, pp. 11 054–11 059.
- [13] I. Vizzo, T. Guadagnino, B. Mersch, L. Wiesmann, J. Behley, and C. Stachniss, "Kiss-icp: In defense of point-to-point icp - simple, accurate, and robust registration if done the right way," *IEEE Robot. Autom. Lett.*, vol. 8, no. 2, pp. 1029–1036, 2023.
- [14] D. Aiger, N. J. Mitra, and D. Cohen-Or, "4-points congruent sets for robust pairwise surface registration," *ACM Trans. Graph.*, vol. 27, no. 3, pp. 1–10, 2008.
- [15] N. Mellado, D. Aiger, and N. J. Mitra, "Super 4pcs fast global pointcloud registration via smart indexing," *Comput. Graph. Forum*, vol. 33, no. 5, pp. 205–215, 2014.
- [16] J. Fan, J. Yang, F. Lu, D. Ai, Y. Zhao, and Y. Wang, "3-points convex hull matching (3pchm) for fast and robust point set registration," *Neurocomputing*, vol. 194, pp. 227–240, 2016.
- [17] J. Fan, J. Yang, Y. Zhao, D. Ai, Y. Liu, G. Wang, and Y. Wang, "Convex hull aided registration method (charm)," *IEEE Trans. Vis. Comput. Graphics*, vol. 23, no. 9, pp. 2042–2055, 2017.
- [18] R. B. Rusu, N. Blodow, and M. Beetz, "Fast Point Feature Histograms (FPFH) for 3D registration," in *Proc. IEEE Int. Conf. Robot. Autom. (ICRA)*. IEEE, 2009, pp. 3212–3217.
- [19] I. Sipiran and B. Bustos, "Harris 3d: a robust extension of the harris operator for interest point detection on 3d meshes," *Vis Comput.*, vol. 27, no. 11, pp. 963–976, 2011.
- [20] J. Li, Q. Hu, and M. Ai, "Point cloud registration based on one-point ransac and scale-annealing biweight estimation," *IEEE Trans. Geosci. Remote Sensing*, vol. 59, no. 11, pp. 9716–9729, 2021.
- [21] P. Shi, S. Yan, Y. Xiao, X. Liu, Y. Zhang, and J. Li, "Ransac back to sota: a two-stage consensus filtering for real-time 3d registration," *IEEE Robot. Autom. Lett.*, vol. 9, no. 12, pp. 11 881–11 888, 2024.
- [22] X. Bai, Z. Luo, L. Zhou, H. Chen, L. Li, Z. Hu, H. Fu, and C.-L. Tai, "Pointdsc: robust point cloud registration using deep spatial consistency," in *Proc. IEEE Conf. Comput. Vis. Pattern Recognit.* Nashville, TN, USA: IEEE, 2021, pp. 15 854–15 864.
- [23] J. Yang, Z. Huang, S. Quan, Z. Qi, and Y. Zhang, "Sac-cot: sample consensus by sampling compatibility triangles in graphs for 3-d point cloud registration," *IEEE Trans. Geosci. Remote Sensing*, vol. 60, pp. 1–15, 2022.
- [24] Z. Chen, K. Sun, F. Yang, and W. Tao, "Sc2-pcr: a second order spatial compatibility for efficient and robust point cloud registration," in *Proc. IEEE Conf. Comput. Vis. Pattern Recognit.*, 2022, pp. 13 211–13 221.
- [25] J. Yang, H. Li, D. Campbell, and Y. Jia, "Go-icp: a globally optimal solution to 3d icp point-set registration," *IEEE Trans. Pattern Anal. Mach. Intell.*, vol. 38, no. 11, pp. 2241–2254, 2016.
- [26] A. Parra Bustos and T.-J. Chin, "Guaranteed outlier removal for point cloud registration with correspondences," *IEEE Trans. Pattern Anal. Mach. Intell.*, vol. 40, no. 12, pp. 2868–2882, 2018.
- [27] W. Chen, H. Li, Q. Nie, and Y.-H. Liu, "Deterministic point cloud registration via novel transformation decomposition," in *Proc. IEEE Conf. Comput. Vis. Pattern Recognit.*, 2022, pp. 6338–6346.
- [28] T. Huang, L. Peng, R. Vidal, and Y.-H. Liu, "Scalable 3d registration via truncated entry-wise absolute residuals," in *Proc. IEEE Conf. Comput. Vis. Pattern Recognit.* Seattle, WA, USA: IEEE, 2024, pp. 27 467–27 477.
- [29] T. Huang, H. Li, L. Peng, Y. Liu, and Y.-H. Liu, "Efficient and robust point cloud registration via heuristics-guided parameter search," *IEEE Trans. Pattern Anal. Mach. Intell.*, vol. 46, no. 10, pp. 6966–6984, 2024.
- [30] T. Joseph, "An alternative proof of euler's rotation theorem," *Math. Intell.*, vol. 42, no. 4, pp. 44–49, 2020.
- [31] X. Zhang, L. Peng, W. Xu, and L. Kneip, "Accelerating globally optimal consensus maximization in geometric vision," *IEEE Trans. Pattern Anal. Mach. Intell.*, vol. 46, no. 6, pp. 4280–4297, 2024.
- [32] M. de Berg, O. Cheong, M. Van Kreveld, and M. Overmars, *Computational Geometry: Algorithms and Applications*. Berlin, Heidelberg: Springer, 2008.
- [33] J. L. Bentley, "Solution to klee's rectangle problems," Carnegie-Mellon Univ., Pittsburgh, PA, Tech. Rep., 1977.
- [34] Bentley and Ottmann, "Algorithms for reporting and counting geometric intersections," *IEEE Trans. Comput.*, vol. C-28, no. 9, pp. 643–647, 1979.

- [35] A. Zeng, S. Song, M. Niessner, M. Fisher, J. Xiao, and T. Funkhouser, “3dmatch: learning local geometric descriptors from rgb-d reconstructions,” in *Proc. IEEE Conf. Comput. Vis. Pattern Recognit.* Honolulu, HI: IEEE, 2017, pp. 199–208.
- [36] C. Choy, J. Park, and V. Koltun, “Fully convolutional geometric features,” in *Proc. IEEE Int. Conf. Comput. Vis.*, 2019.
- [37] S. Huang, Z. Gojcic, M. Usvyatsov, A. Wieser, and K. Schindler, “Predator: registration of 3d point clouds with low overlap,” in *Proc. IEEE Conf. Comput. Vis. Pattern Recognit.*, 2021, pp. 4265–4274.
- [38] Z. Qin, H. Yu, C. Wang, Y. Guo, Y. Peng, and K. Xu, “Geometric transformer for fast and robust point cloud registration,” in *Proc. IEEE Conf. Comput. Vis. Pattern Recognit.* New Orleans, LA, USA: IEEE, 2022, pp. 11 133–11 142.
- [39] M. A. Fischler and R. C. Bolles, “Random sample consensus: a paradigm for model fitting with applications to image analysis and automated cartography,” *Commun. ACM*, vol. 24, no. 6, pp. 381–395, 1981.
- [40] C. Choy, W. Dong, and V. Koltun, “Deep global registration,” in *Proc. IEEE Conf. Comput. Vis. Pattern Recognit.* Seattle, WA, USA: IEEE, 2020, pp. 2511–2520.
- [41] Y. Wang, P. Zhou, G. Geng, L. An, and Y. Liu, “Ccg: end-to-end point cloud registration,” *IEEE Robot. Autom. Lett.*, vol. 9, no. 1, pp. 435–442, 2024.
- [42] Y. Yang, J. Fan, L. Shao, M. Lei, T. Fu, D. Ai, D. Xiao, H. Song, Y. Lin, and J. Yang, “Landmark and pose prediction in occluded facial point cloud via explicit joint feature fusion network,” *IEEE Trans. Circuits Syst. Video Technol.*, pp. 1–14, 2025.
- [43] H. Yang, J. Shi, and L. Carlone, “Teaser: fast and certifiable point cloud registration,” *IEEE Trans. Robot.*, vol. 37, no. 2, pp. 314–333, 2021.
- [44] X. Zhang, J. Yang, S. Zhang, and Y. Zhang, “3D registration with maximal cliques,” in *Proc. IEEE Conf. Comput. Vis. Pattern Recognit.*, Vancouver, BC, Canada, 2023, pp. 17 745–17 754.
- [45] D. Barath and J. Matas, “Graph-cut RANSAC,” in *Proc. IEEE Conf. Comput. Vis. Pattern Recognit.* Salt Lake City, UT, USA: IEEE, 2018, pp. 6733–6741.
- [46] Z. Chen, K. Sun, F. Yang, L. Guo, and W. Tao, “Sc2-pcr++: rethinking the generation and selection for efficient and robust point cloud registration,” *IEEE Trans. Pattern Anal. Mach. Intell.*, vol. 45, no. 10, pp. 12 358–12 376, 2023.
- [47] Á. Parra, T.-J. Chin, F. Neumann, T. Friedrich, and M. Katzmann, “A practical maximum clique algorithm for matching with pairwise constraints,” 2019.
- [48] D. Eppstein, M. Löffler, and D. Strash, “Listing all maximal cliques in sparse graphs in near-optimal time,” in *Proc. Int. Symp. Algorithms Comput. (ISAAC)*. Berlin, Heidelberg: Springer, 2010, vol. 6506, pp. 403–414.
- [49] R. I. Hartley and F. Kahl, “Global optimization through rotation space search,” *Int. J. Comput. Vis.*, vol. 82, no. 1, pp. 64–79, 2009.
- [50] A. Parra Bustos, T.-J. Chin, A. Eriksson, H. Li, and D. Suter, “Fast rotation search with stereographic projections for 3d registration,” *IEEE Trans. Pattern Anal. Mach. Intell.*, vol. 38, no. 11, pp. 2227–2240, 2016.
- [51] X. Li, H. Cao, Y. Liu, X. Liu, F. Zhang, and A. Knoll, “Efficient and deterministic search strategy based on residual projections for point cloud registration with correspondences,” *IEEE Trans. Intell. Veh.*, vol. 9, no. 11, pp. 7421–7436, 2024.
- [52] J. P. Snyder, *Map Projections: A Working Manual*. Washington, D.C.: U.S. Government Printing Office, 1987.
- [53] D. de Menezes, D. Prata, A. Secchi, and J. Pinto, “A review on robust m-estimators for regression analysis,” *Comput. Chem. Eng.*, vol. 147, p. 107254, 2021.
- [54] A. Geiger, P. Lenz, and R. Urtasun, “Are we ready for autonomous driving? the kitti vision benchmark suite,” in *Proc. IEEE Conf. Comput. Vis. Pattern Recognit.* Providence, RI: IEEE, 2012, pp. 3354–3361.
- [55] B. Curless and M. Levoy, “A volumetric method for building complex models from range images,” in *Proc. ACM SIGGRAPH*. ACM, 1996, pp. 303–312.
- [56] R. Hartley, J. Trunpf, Y. Dai, and H. Li, “Rotation averaging,” *Int. J. Comput. Vision*, vol. 103, no. 3, pp. 267–305, 2013.
- [57] G. Guennebaud, B. Jacob *et al.*, “Eigen v3,” <http://eigen.tuxfamily.org>, 2010.
- [58] R. B. Rusu and S. Cousins, “3d is here: Point cloud library (pcl),” in *Proc. IEEE Int. Conf. Robot. Autom. (ICRA)*. Shanghai, China: IEEE, 2011, pp. 1–4.
- [59] J. L. Blanco and P. K. Rai, “nanoflann: a C++ header-only fork of FLANN, a library for nearest neighbor (NN) with kd-trees,” <https://github.com/jlblancoc/nanoflann>, 2014.
- [60] Q.-Y. Zhou, J. Park, and V. Koltun, “Open3D: A modern library for 3D data processing,” *Arxiv:1801,09847*, 2018.
- [61] J. Straub, O. Freifeld, G. Rosman, J. J. Leonard, and J. W. Fisher, “The manhattan frame model-manhattan world inference in the space of surface normals,” *IEEE Trans. Pattern Anal. Mach. Intell.*, vol. 40, no. 1, pp. 235–249, 2018.
- [62] H. Lim, S. Yeon, S. Ryu, Y. Lee, Y. Kim, J. Yun, E. Jung, D. Lee, and H. Myung, “A single correspondence is enough: robust global registration to avoid degeneracy in urban environments,” in *Proc. IEEE Int. Conf. Robot. Autom. (ICRA)*. Philadelphia, PA, USA: IEEE, 2022, pp. 8010–8017.